IN THE LAND OF HOBITSS WHERE THE SLOW SLIP EVENTS LIE

A Thesis

presented to

the Faculty of the Graduate School

at the University of Missouri-Columbia

In Partial Fulfillment

of the requirements for the Degree

Master of Science

---

by

\RYAN MICHAEL YOHLER Dr.

Noel Bartlow, Thesis Supervisor

MAY 2018

The undersigned, appointed by the dean of the Graduate School, have examined the thesis entitled

IN THE LAND OF HOBITSS WHERE THE SLOW SLIP EVENTS LIE

presented by Ryan Michael Yohler, a candidate for the degree of Master of Science, and hereby certify that, in their opinion, it is worthy of acceptance.

_____

Dr. Noel Bartlow

_____

Dr. Mian Liu

_____

Dr. Stephen Montgomery-Smith

ACKNOWLEDGEMENTS

I would like to thank my thesis advisor, Dr. Noel Bartlow, for her continuous support during my time at the University of Missouri. In addition, I would like to thank my NSF EAPSI hosts, Dr. Laura Wallace and Dr. Charles Williams, who provided one of the best learning experiences a graduate student could have. I would also like to thank my committee, Dr. Mian Liu and Dr. Stephen Montgomery-Smith, for being excellent teachers and mentors. In addition to all of the friends I've made at the University of Missouri, I would like to thank my parents, my friends back home, and my undergraduate advisor, for providing guidance and reassurance. And finally, my dog Max, who always welcomed me home during stressful days in the office.

TABLE OF CONTENTS

List of Illustrations

Figure Page

List of Tables

Nomenclature

1. Continuous Global Positioning System (cGPS)
2. Slow Slip Events (SSEs)
3. Absolute Pressure Gauges (APGs)
4. Green's Functions (GFs)
5. Probability Density Function (PDF)
6. Cumulative Density Function (CDF)
7. Credible Interval (CI)

IN THE LAND OF HOBITSS WHERE THE SLOW SLIP EVENTS LIE

Ryan Michael Yohler

Dr. Noel Bartlow, Thesis Supervisor

Abstract

Continuous GPS campaigns over the last few decades have brought an unprecedented look into the behaviors and processes that drive subduction zones. A major discovery during this time has been Slow Slip Events, which release tectonic stress over longer periods than earthquakes. Although slow slip occurs in a variety of places along a subduction interface, a particular place of interest are those slow slip patches that occur offshore and near the subduction trench since these may trigger damaging tsunami earthquakes. While onshore GPS have been able to model these offshore events with some resolution, offshore resolution is always limited with onshore geodetic networks. Recent advances in geodesy have placed seafloor geodetic instruments directly above the slipping patches. I evaluate the time-dependent behavior and range of potential seismic moments of slow slip event that took place offshore Gisborne New Zealand in 2014 while incorporating realistic elastic properties and co-inverting onshore and offshore instruments. The results indicate a significant decrease in uncertainty when using the offshore data while the heterogenetic properties result in an increase. While the realistic elastic properties show a decrease in peak during the slow slip event, they create a higher seismic moment. In addition, the addition of offshore data moves the onset of the event several days sooner and significantly increases the most likely seismic moment. The study showcases the use of newly available seafloor geodetic data for resolving offshore deformation.

CHAPTER 1:

INTRODUCTION

1.1 Slow Slip Events

Continuous GPS (cGPS) campaigns have the capability to monitor deformation on the surface in near-real time. Decade long catalogs of data from these sites have provided incredible insight into subduction zone and tectonic deformation processes, including the temporal and spatial relationships that drive deformation events. These investigations have led to the discovery of slow slip events (SSEs), which are aseismic fault slip and sometimes associated with non-volcanic, tectonic tremor. SSEs, like earthquakes, accommodate slip on faults higher than typical plate-rates and can release significant moment. However, unlike earthquakes, SSEs have longer durations, lasting for hours up to years, and do not produce damaging seismic waves or tsunamis.

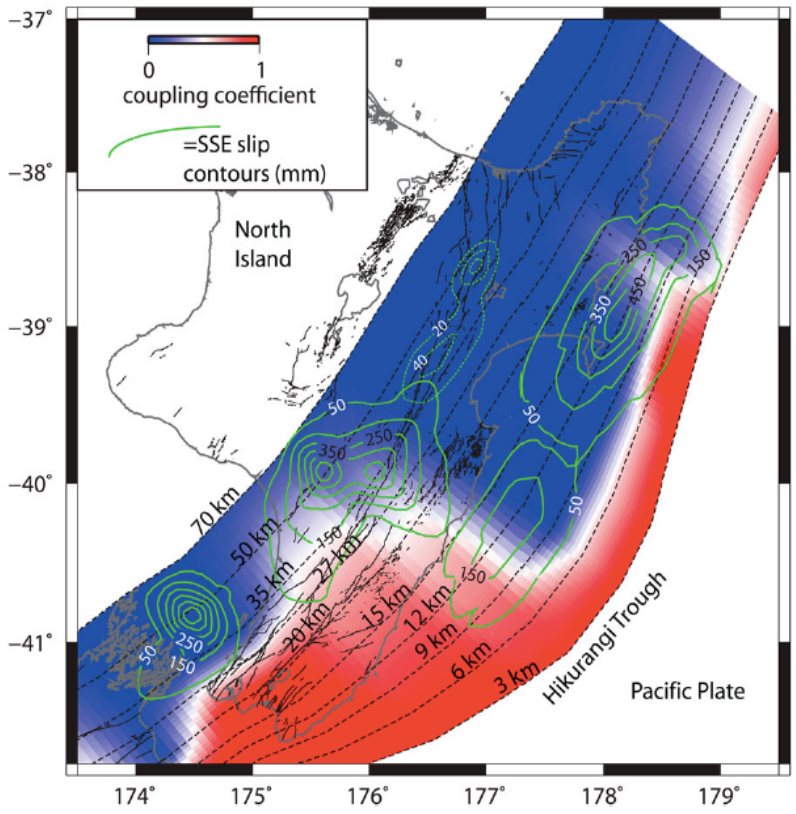

Figure 1.1: Distribution of seismic coupling along the Hikurangi subduction margin. The green contours, showing SSE areas, occur along downdip limit of strong coupling. Taken from Wallace et al. 2016

Most SSEs identified to date occur on subduction zone plate interfaces, such as those in New Zealand, Japan, Mexico, and Cascadia (*Schwartz and Rokosky 2007*). In many cases, they appear to happen adjacent to locked regions where large megathrust earthquakes occur (e.g. *Wallace et al. 2016, Fujie et al. 2013, Bartlow et al. 2014, Schmidt and Gao 2010*). In New Zealand, there is a strong correlation between SSE locations and the downdip limit of the locked zone on the Hikurangi Subduction interface (**Figure 1.1)**. The depth of the locked zone, and the depth of the SSEs, vary significantly along strike. The duration of the SSEs is a function of their depths, with deeper SSEs lasting longer than shallow ones (*Wallace et al 2016*).

A conceptual model of the relationship between SSEs, the locked zone, and megathrust earthquakes is shown in **Figure 1.2** (*Power et al. 2016*). As the Pacific Plate is colliding with and subducting underneath the Australian plate, frictional locking occurs on the plate interface preventing that region from slipping. A large buildup of stress occurs on the locked portion of the subduction interface. Additionally, when an SSE occurs, the area of the event sees a decrease in stress while the area surrounding the event sees an increase in stress. Thus, since SSEs occur downdip from the locked region, they can create additional stress within the locked region. This increased stress in the locked region is eventually relieved in large, megathrust earthquakes, and previous studies have correlated SSEs to these events. For example, the 2011 M_W 9.0 Tohoku-Oki earthquake was preceded by a slow slip sequence that migrated along the subduction trench towards the epicenter (e.g *Kato et al. 2012; Ito et al., 2013*). This pattern was seen in New Zealand, where three SSEs occurred between June 2015 and August 2016 that preceded the 2016 M_W 7.1 Te Araroa earthquake (*Koulali et al. 2017*). Interactions between SSEs

and earthquakes can be complex and go both ways. For example, the 2016 M_W 7.8 Kaikōura earthquake in New Zealand dynamically triggered SSEs as far as 600km away (*Wallace et al. 2016*). Thus, it is important to properly characterize the amount and extent of SSE slip, both in space and time, to properly constrain the overall slip budget and potential for large earthquakes and tsunami producing earthquakes in a subduction zone.

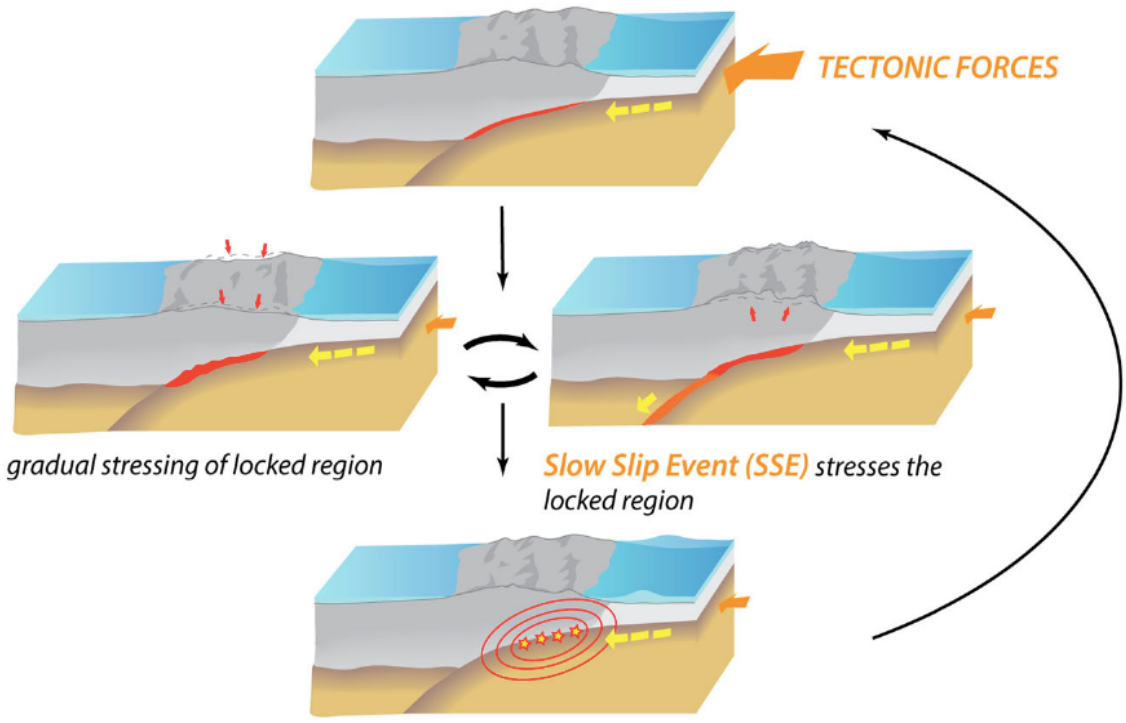

Figure 1.2: Conceptual model showing the megathrust earthquake cycle. Stress from tectonic forces accumulate in locked patches of a subduction zone during SSE and inner-SSE periods. The SSEs occur downdip from the locked region and additionally stress the locked region. Taken from Power et al. 2016.

This study investigates a specific SSE off the east coast of New Zealand in the Gisborne area (**Figure 1.3**). This SSE patch, which I will denote the Gisborne SSE patch, occurs close to the subduction trench. Earthquake ruptures in the near trench region are

especially hazardous because of their increased ability to create tsunamis. For example, on March 26th and May 17th 1947, two earthquakes around M_W 7.1 occurred close to the Gisborne SSE patch and created tsunami run ups up to 6 m high (**Figure 1.3**). Although the locations for the 1947 tsunami earthquakes are extremely uncertain, some locations estimates are available from New Zealand's GeoNET (https://www.geonet.org.nz/tsunami/story/1543047). Whether or not these earthquakes were linked to SSEs is entirely unknown.

The Gisborne SSE patch is shallow (<15km) and slips over a two-week time period at least two times a year, with significant variability in event size and repeat interval. Until very recently, researchers have been limited to using onshore GPS measurements to study the offshore Gisborne SSE patch, significantly limiting resolution in the near-trench region. Resolving the extent of SSEs offshore is extremely important for characterizing the extent of the locked zone, and thus the future tsunami hazards in Gisborne region.

In order to produce models with better resolution near the subduction trench, offshore instruments including Absolute Pressure Gauges (APGs) were deployed as part of the Hikurangi Ocean Bottom Investigation of Tremor and Slow Slip (HOBITSS) experiment over the Gisborne SSE patch in 2014. During this time, the HOBITSS network recorded the 2014 Gibsorne SSE (**Figure 1.4**). *Wallace et al. 2016* originally published these APG data as well as the first static co-inversions using the onshore GPS and offshore APG data (**Figure 1.5**). This was the first detailed view of a shallow, offshore SSE using APG data. These data have been converted to vertical displacement of the seafloor, and have been processed to remove long-term drift, and low pass filtered to

reduce oceanographic and tidal effects**.** Oceanographic effects were additionally removed by differencing data with two stations on the incoming plate.

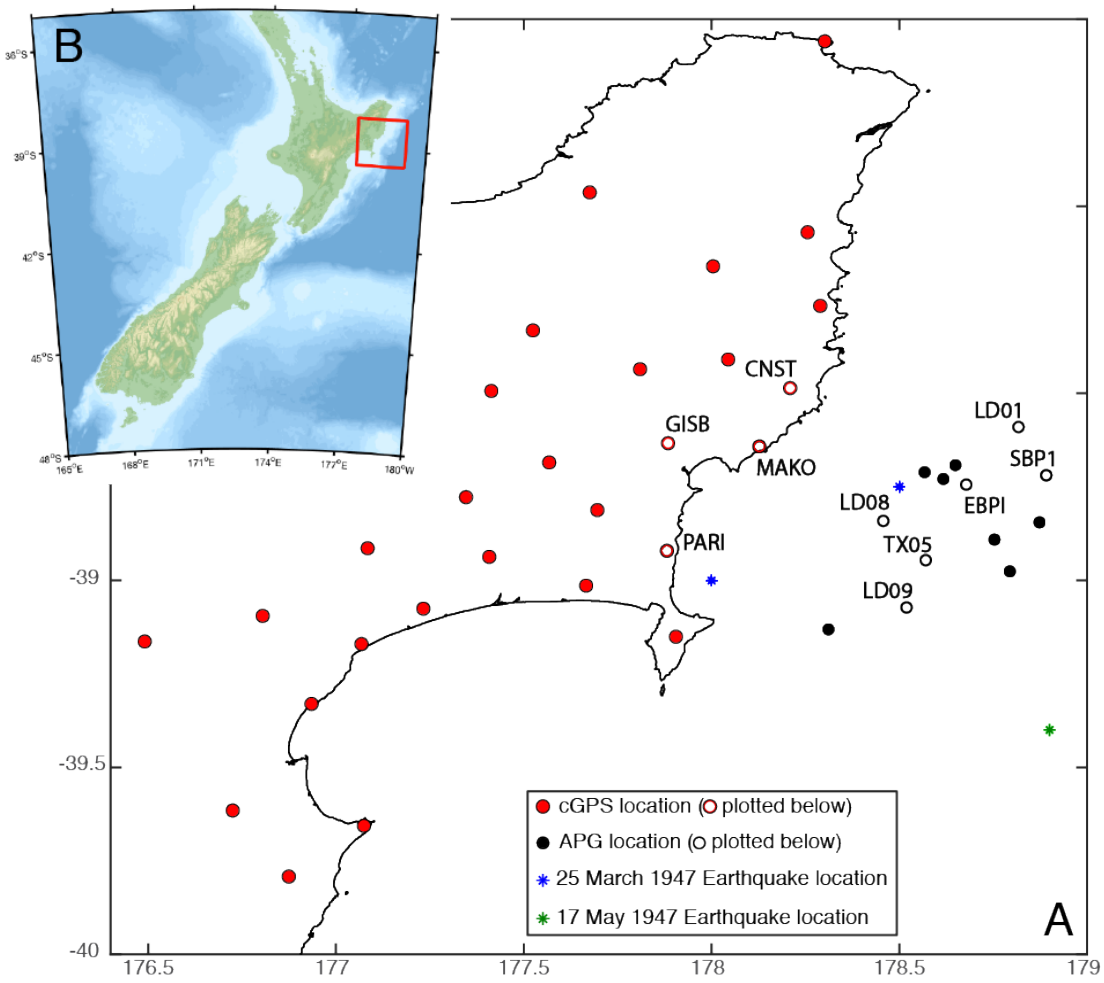

Figure 1.3: Station coverage map with the estimated locations of 1947 Tsunami earthquakes. Red circles are cGPS locations and black circles are APG locations. Two estimates of the location for the March 25th 1947 tsunami earthquake are shown as blue stars, while the estimated location May 17th event is shown as a green star.

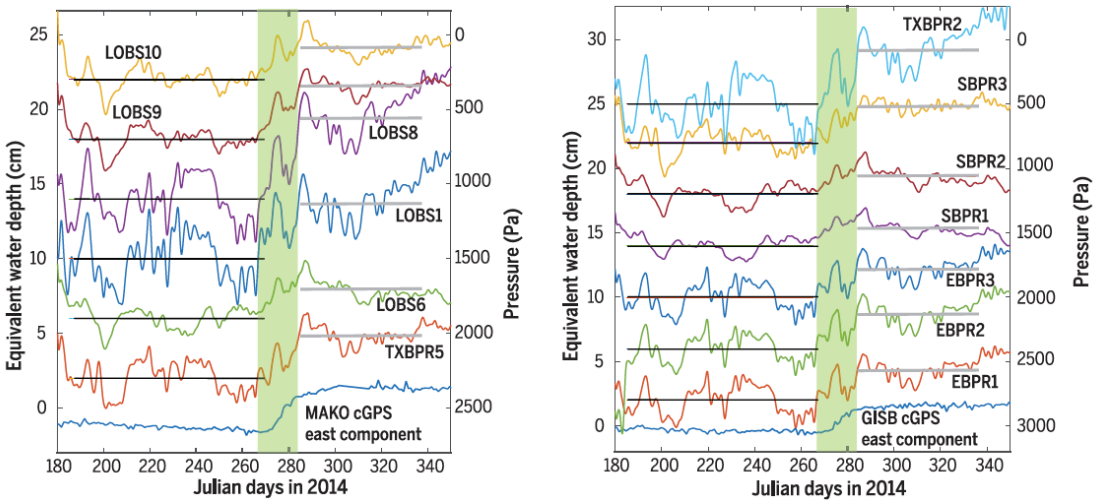

Figure 1.4: Processed APG time-series from Wallace et al. 2016 showing 'Equivalent water depth (cm)' and 'Pressure(Pa)'. Equivalent water depth is defined such that positive values represent seafloor uplift. Green bar highlights the time of the 2014 Gisborne SSE.

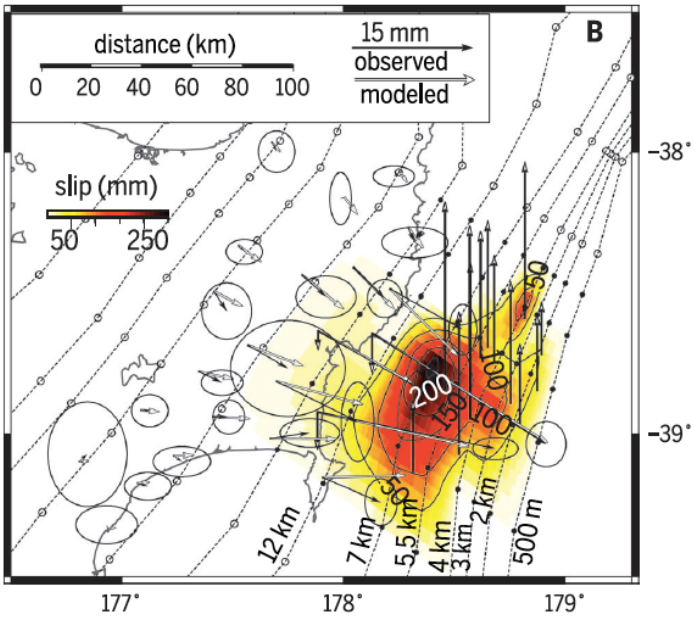

Figure 1.5: Static inversion of cGPS and APG data for slip during the 2014 Gisborne SSE (Wallace et al. 2016).Offshore arrows indicate APG uplift. Dotted lines indicate contours of the subduction interface. Peak slip is around 25 cm.

While the *Wallace et al. 2016* study detailed the importance of using APG data for investigating this offshore SSE, the inversion was static and provided no details of its behavior. Here I investigate the time-dependent slip distribution and propagation during

the 2014 SSE by joint time-dependent inversion of the HOBITSS APG data and onshore cGPS data. My aim is to infer how slip-rate and slip along the plate interface vary over time as well as trying to capture any migration patterns that might be present. This study is the first-time seafloor geodetic data has been incorporated into a time-dependent slip model.

Additionally, I determine the proper noise model for the APG data, and quantify how inclusion of this data reduces slip uncertainty offshore. I also investigate the range of models can fit the GPS and APG data within a given uncertainty using a moment bounding approach following *Murray and Segall, 2007, and Maurer et al. 2017*.

1.2 Tectonic Setting of New Zealand.

The Hikurangi subduction zone accommodates the westward-moving pacific plate along the Eastern margin of the north island of New Zealand. The plate convergence is oblique and the rate of convergence varies from less than 3 to almost 6 cm/year along the margin (**Figure 1.6**). Shallow SSEs occur near the trench offshore from Gisborne, New Zealand every 18-24 months at a depth of 10-15km. The size and repeat interval of these SSEs are variable and not as time-predictable as SSEs in other regions such as Cascadia (e.g. *Schmidt and Gao 2010, Brudzinski and Allen 2007*).

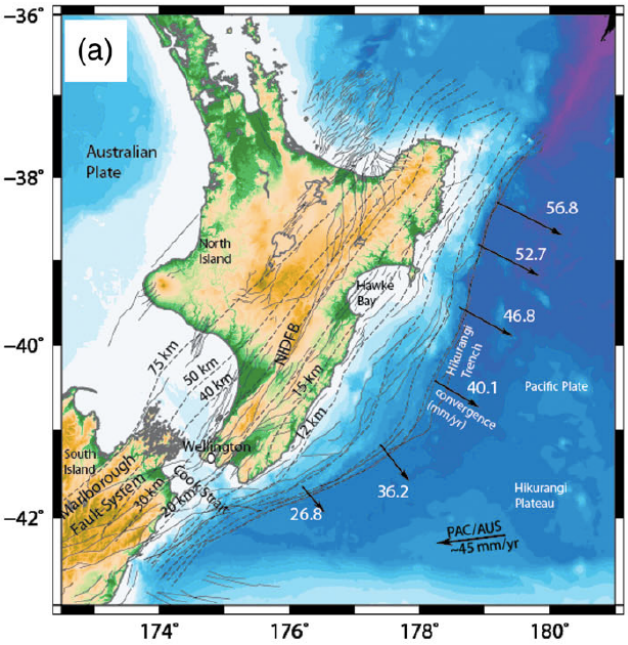

Figure 1.6: Tectonic setting of New Zealand. Dotted lines are subduction interface contours. Plate convergence is ~45 mm/yr Taken from Power et al. 2016.

CHAPTER 2:

TIME-DEPENDENT MODELS:

NETWORK INVERSION FILTER (NIF)

2.1 Network Inversion Filter Method

This study uses a Kalman-filter based time-dependent slip inversion method known as the Network Inversion Filter (NIF) (*Segall & Mathews 1994; Miyazaki et al., 2006)*. The NIF fits GPS time series using:

$$X(t) = X(0) + Gs(t) + Ff(t) + L(t) + \in \quad (1)$$

Where $X(t)$ is a vector of GPS station displacements at time t, $X(0)$ is a vector containing initial GPS (and APG) displacements, G is a pre-calculated matrix of Green's functions which maps slip from triangular fault patches to GPS and APG displacements, $s(t)$ is the slip vector containing slip on each triangular fault patch at time t, $F(t)$ is a matrix representing whole network translation, $f(t)$ is the time-dependent reference frame correction, $L(t)$ is a vector containing the random walk (RW) benchmark wobble value at each station at time t, and $\in$ is white noise. Slip on each triangle is constrained to match the plate interface slip directions of *Wallace et al., 2004*.

A time window of 100 days from 8/26/2014 – 12/3/2014 was selected in order to capture the full SSE. The NIF runs through the data first forwards, then backwards. At each time step t, the NIF first predicts slip based on the previous time step's estimates of slip (s(t-*1*)) and slip rate ($\dot{s}$(t-1)). It then updates this predication with the data. Following the forward steps, the NIF performs a backward smoothing step from the ending time step back to the beginning, which results in the model being dependent on all data at all times t. The NIF incorporates two smoothing parameters, α (temporal smoothing which effectively weights the prediction step versus the data update step) and γ (spatial

smoothing parameter that controls how well the model fits the data versus minimizing the discrete laplacian of the slip distribution). In model comparisons shown here (with different elastic properties and with or without APG data), alpha and gamma values are the same between models and are chosen by trial-and-error from looking at model fits to the data. The variables, $L(t)$, and $f(t)$, $s(t)$, and it's time derivative $\dot{s}(t)$ are stored in a state vector which is solved for at each time step. The resulting $s(t)$ and $\dot{s}(t)$ are daily values of cumulative slip and slip-rate on each triangular subfault that can be averaged over longer time periods. Inter-SSE velocities (secular velocities) and seasonal signals are removed from the data before the inversion (*Bartlow et al. 2014*).

For the APG data, I use the processed time series described in *Wallace et al 2016***.** The processed APG time series still include significant common-mode noise across APG stations, which is a result of left over oceanographic noise after differencing with stations on the incoming plate (**Figure 2.1**). This is likely due to geometry, as both stations on the incoming plate are located to the East of the network. Because all the stations may potentially record the slow slip event, removing a network average may remove tectonic signals of interest in addition to the common mode error. I therefore add an additional APG-specific reference frame correction term to the NIF. The APG reference frame correction term accommodates this common mode noise, while the inclusion of the onshore cGPS data helps differentiate common-mode noise from tectonic signals. The APG reference frame correction variance was selected based on the variance of the processed APG time series as 20 mm, significantly larger than the 5 mm value used for cGPS data.

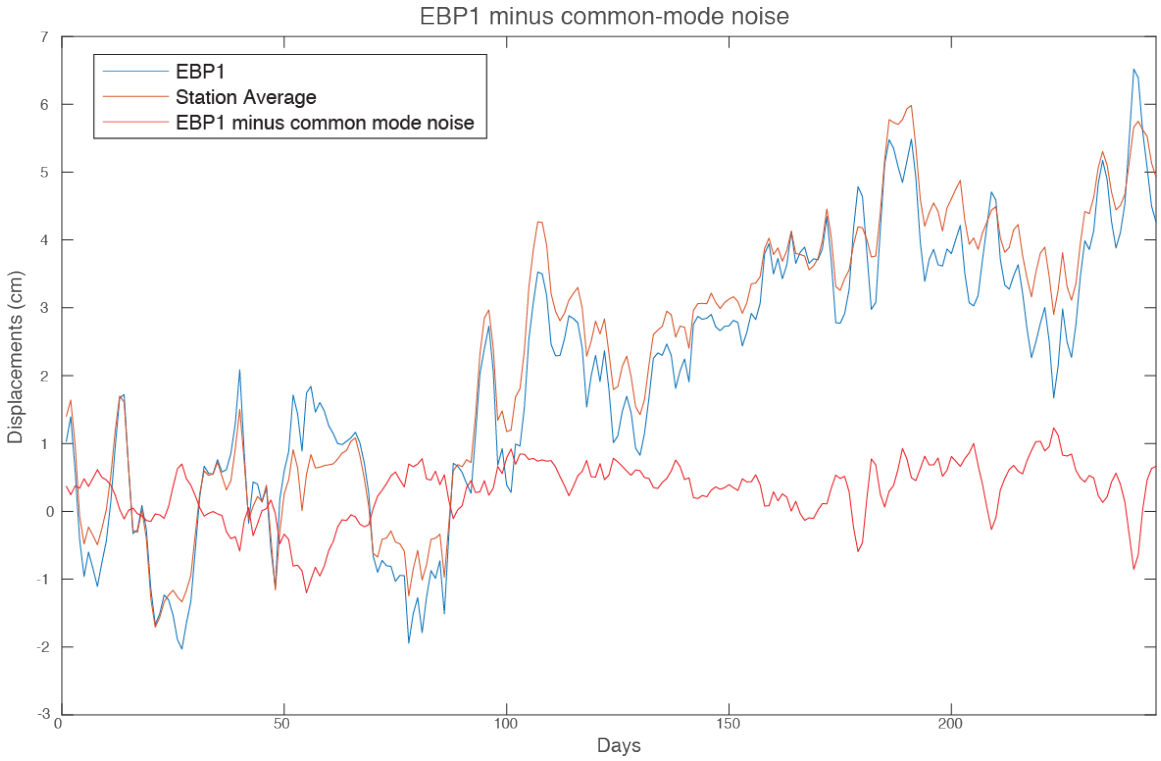

Figure 2.1: APG displacements for EBP1 (blue), averaged displacements over all stations (orange), and EBP1 minus the station average (red). A quiet period before the SSE was taken from the red time series and used in the spectral analysis (Figure 8) to determine the correct random walk variable.

The random walk noise (benchmark wobble) amplitude (*f(t)* in **equation 1**) is considerably higher for the APGs (12.5 mm/$\sqrt{yr}$) compared to the cGPS value used by this and prior studies (1 mm/$\sqrt{yr}$). The APG random walk was calculated by spectral analysis of timeseries from a representative station. To correct for common-mode noise in this spectral analysis, I remove a network average before taking a power spectrum during a quiet period and matching to a model spectrum including random walk and white noise (**Figure 2.1 & 2.2**). A random walk amplitude of 12.5 mm/$\sqrt{yr}$ was selected as a good match to the data, especially at lower frequencies which represent most of the spectral power. As the actual spectral decay of the data is not exactly a random walk, the data exceeds the random walk model at higher frequencies. In order to focus on the SSE

event and decrease computation time, I limited the cGPS stations to those used in *Wallace et al. 2016.*

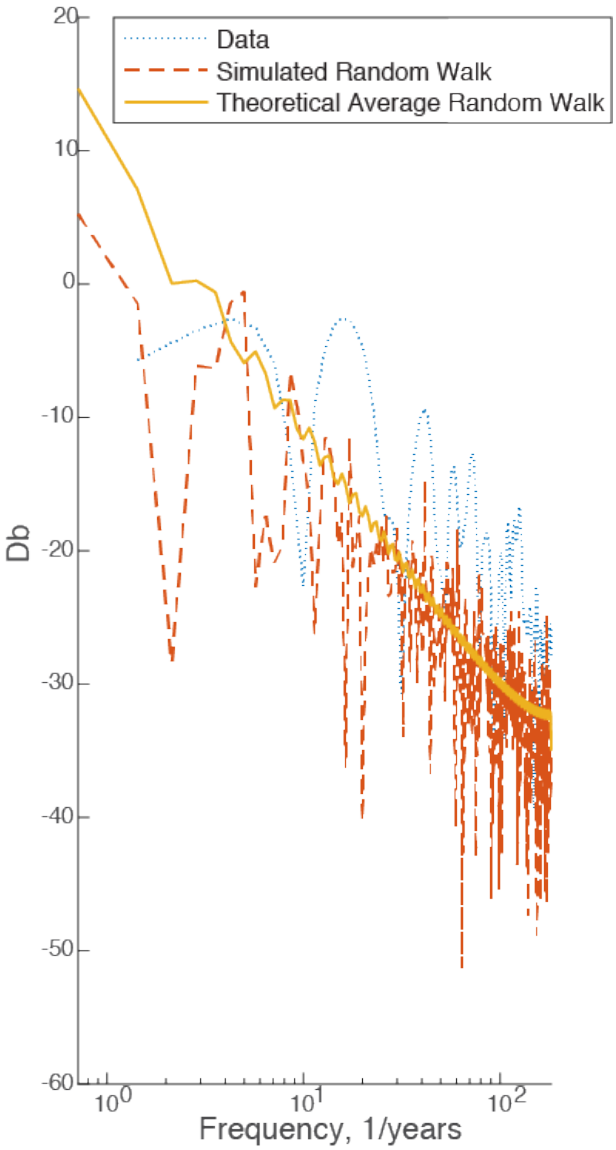

Figure 2.2: Spectral analysis of APG data and comparison to random walk spectra with an amplitude of 12.5 mm/sqrt yr. Blue is the data (EBP1 time series minus common mode noise), red is a single simulated random walk time series, and yellow is a theoretical average random walk spectrum.

I use both homogenous and heterogeneous elastic properties to construct my Green's functions (*G* matrix in **equation 1**). Both sets of Green's functions were generated using the PyLith finite element code. The heterogeneous Green's functions use

material properties (shear modulus and density) inferred from the New-Zealand wide seismic velocity model (*Eberhart-Philips et al. 2010; Williams 2018*). Since the seismic velocity along the outer forearc overlying the Pacific plate has been shown to be particularly low while displaying elastic changes along the Northern Hikurangi margin, the need for heterogeneous elastic properties is exemplified (*Bassett et al. 2010, McTigue and Segall, 1988; Williams and Wadge, 1998; 2000; Cayol and Cornet, 1998*).

The inclusion of heterogeneous Greens functions in past inversions have shown a change in slip amplitudes by 20-40%, and should represent a more realistic elastic response (*Williams and Wallace 2015*). This is especially important for constraining the total slip budget of the interface in the near-trench region. The combination of the APG data and heterogeneous Greens functions used in this study should provide the most accurate slip model of a shallow SSE to date.

A comparison between the different GPS and APG responses to uniform slip on the plate interface in the Gisborne region using the two sets of Green's functions can be found in **Figure 2.3**. The comparison uses the basic forward model,

$$Gs = d \qquad (2)$$

where G and s are described in **equation 1** and d is the surface response of the cGPS and APG stations (plotted in **Figure 2.3**). For this comparison, unit slip of 1m is applied to the entire subduction interface. **Figure 2.3** shows the East and North components of cGPS and Vertical component (plotted as pointing North) for the APG stations.

With the exception of a few stations, the majority of the cGPS stations respond to unit slip with the heterogeneous Green's Functions (red arrows, **Figure 2.3**) by displacing in a more South-West direction and generally tend to have slightly higher displacements than in the homogeneous case (blue arrows). For the APG data, the magnitudes have almost the opposite response as the cGPS, with the homogeneous elastic properties creating a larger displacement than the heterogeneous Green's functions at most stations.

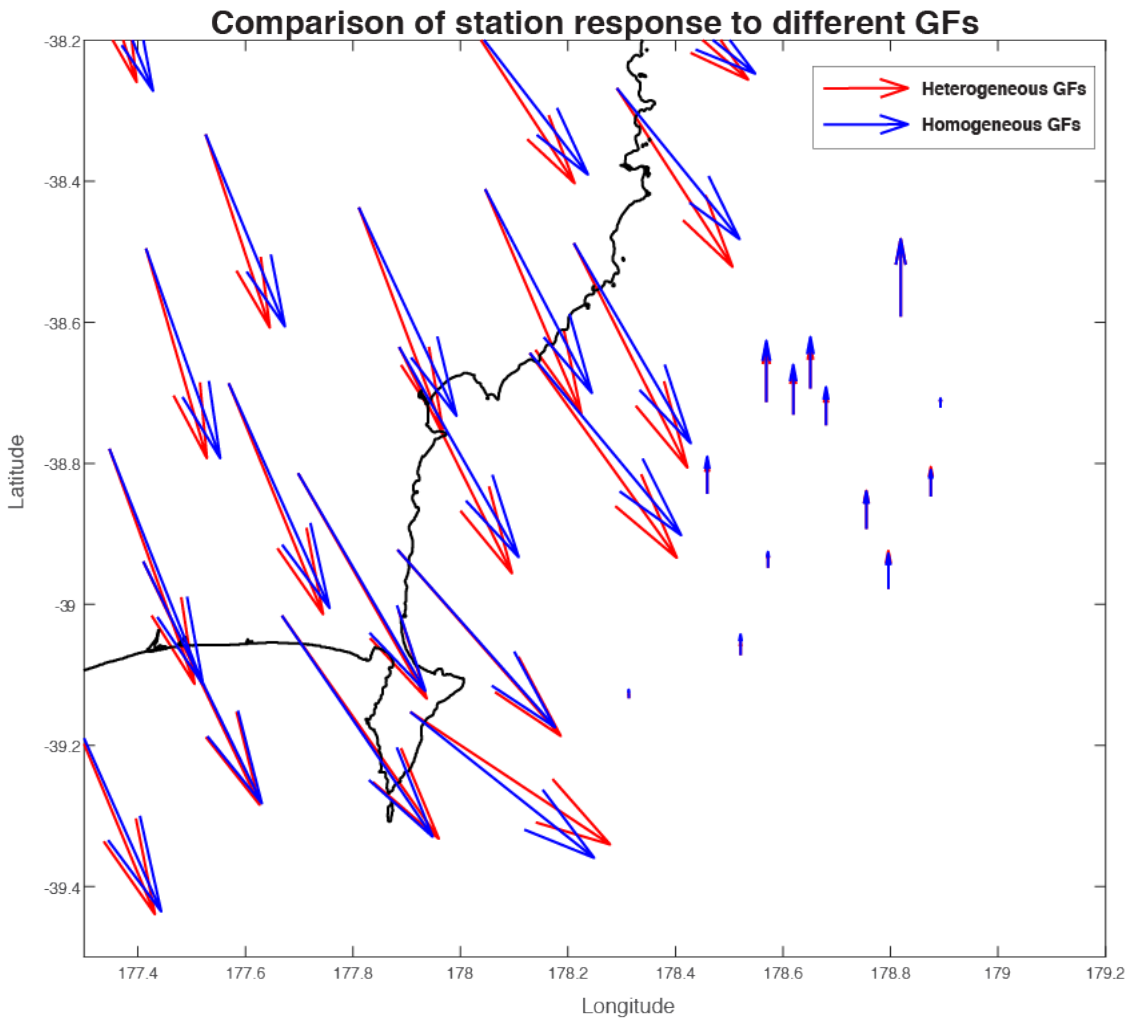

Figure 2.3: Homogeneous (blue) vs Heterogeneous (red) elastic properties and how they change both cGPS and APG responses. cGPS vectors are both E and N components, where APG is depicting vertical displacements.

2.2 Network Inversion Filter Results

Characterizing the distribution of total slip during the 2014 Gisborne SSE provides important constraints on the slip budget in this region. The most physically accurate, and therefore preferred, time-dependent model of the 2014 Gisborne SSE is obtained by using both onshore cGPS and offshore APG data, and using Green's functions that incorporate heterogeneous elastic properties. In order to understand the effects of the inclusion of the APG data and heterogeneous Green's functions on the NIF modeling, I conduct 4 separate inversions using the homogenous (uniform elastic properties) and heterogeneous (realistic elastic properties) Green's functions with and without the inclusion of APG data. **Figure 2.4** highlights the differences in total slip distribution found by the NIF when using the homogenous and heterogeneous Green's Functions as well as with and without the inclusion of the offshore APG data.

The use of the heterogeneous Green's Functions causes the slip distribution to move northward compared to models using homogenous Green's functions. This is true in models both without and with the APG data. The inclusion of the APGs with homogenous Green's Functions caused a decrease in total slip during the SSE, while with the heterogeneous Green's Functions, the APGs caused an increase in slip.

Table 2.1 summarizes the peak slip amplitude and related seismic potency. Seismic potency is similar to the seismic moment (**equation 3**) but is not multiplied by the shear modulus. Potency was used here for comparisons with *Wallace et al. 2016* (**Figure 1.5**) and *Williams and Wallace 2018*. *Wallace et al. 2016,* which was a static co-inversion with homogeneous elastic properties and APGs, had a peak amplitude of 23.2 cm, where the NIF inversion of the same case is nearly identical with 23.73 cm. However, the static

co-inversions with heterogeneous elastic properties and the inclusion of APGs from *Williams and Wallace 2018* had a much higher slip amplitude (29.1 cm) compared to the NIF (23.41 cm).

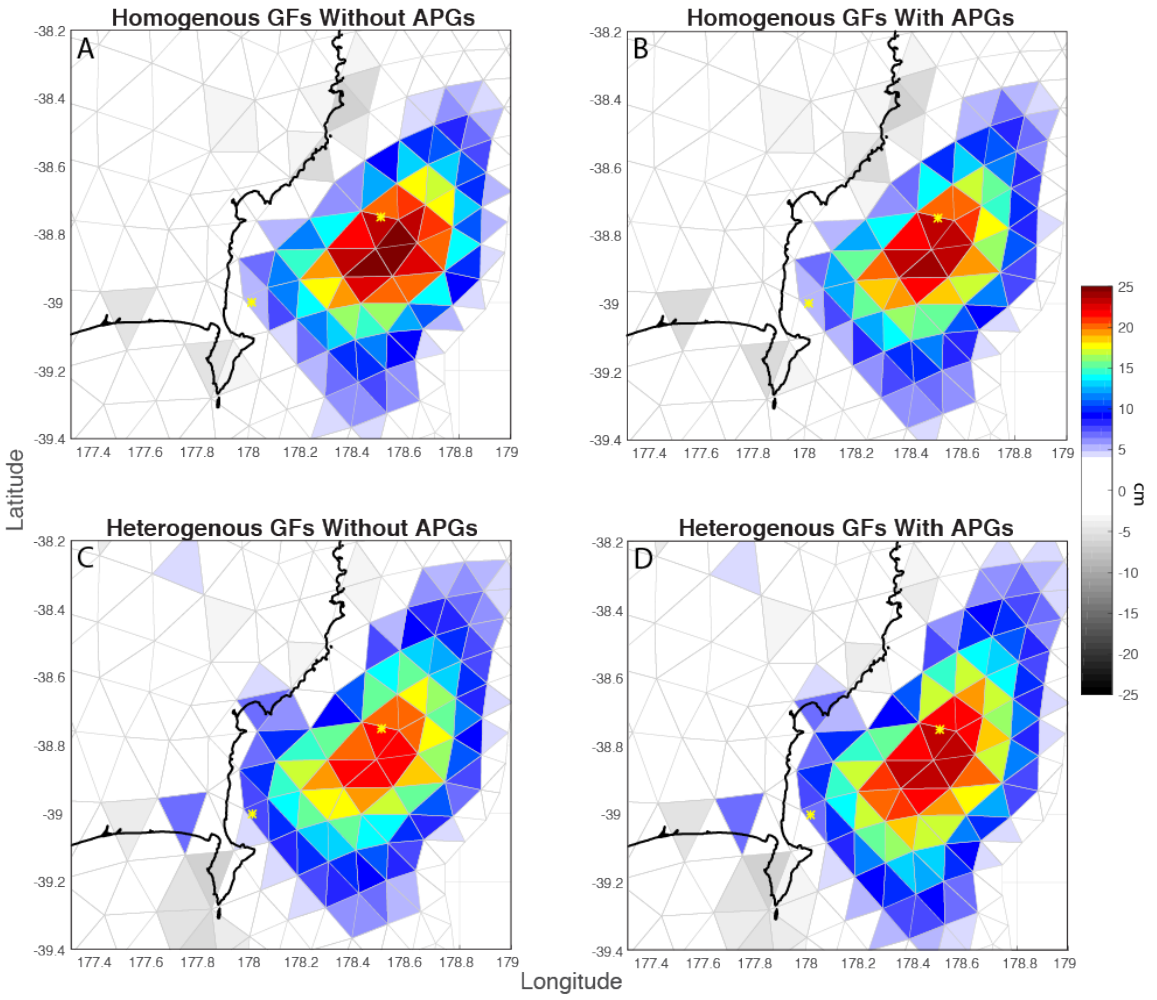

Figure 2.4: Total slip during the Gisborne SSE showing differences between Homogenous (a&b) and Heterogeneous (c&d) elastic properties and inversions without APG data (a&c) and with APG data (b&d). The two estimated locations of the March 25th 1947 tsunami earthquake are plotted as yellow stars. The May 17th earthquake plots outside of the mesh to the east and is not included here.

The major difference between the NIF runs and those of the other two studies is the seismic potency. For the homogeneous case with similar amplitudes, the seismic potency is higher. Even when the amplitude is much smaller in the heterogeneous case, the seismic potency is still larger. This difference comes from comparing the spatial distribution of the slip patch, as The NIF results in a much wider area of slip.

Table 2.1: Summary of NIF results.

Model	**Peak Slip (cm)**	**Seismic potency (m^3)/seismic moment (Nm)**	**% Potency difference from reference model**
Homogenous			
cGPS	25.19	$7.10\ x\ 10^8 / 2.13\ x\ 10^{19}$	0.0
cGPS + APGs	23.73	$6.86\ x\ 10^8 / 2.058\ x\ 10^{19}$	-0.0437
Wallace et al. 2016	23.2	$5.34\ x\ 10^8 / 1.60\ x\ 10^{19}$	
Heterogeneous			
cGPS	21.55	$7.74\ x\ 10^8 / 2.32\ x\ 10^{19}$	17.75
cGPS + APGs	23.41	$8.59\ x\ 10^8 / 2.58\ x\ 10^{19}$	32.32
Williams and Wallace 2018	29.1	$7.79\ x\ 10^8 / 2.34\ x\ 10^{19}$	

Figure 2.5 highlights the differences in total slip among models when you difference them. For the homogeneous models (**2.5 A**), the APGs cause a decrease in slip offshore and away from the trench, whereas the heterogeneous case added more slip offshore and southward (**2.5 B**). When comparing the differences between both the homogeneous and the heterogeneous (**2.5 C** and **2.5 D**), both cases show that the heterogeneous Green's functions had significantly less slip directly offshore and favored more slip closer to the trench.

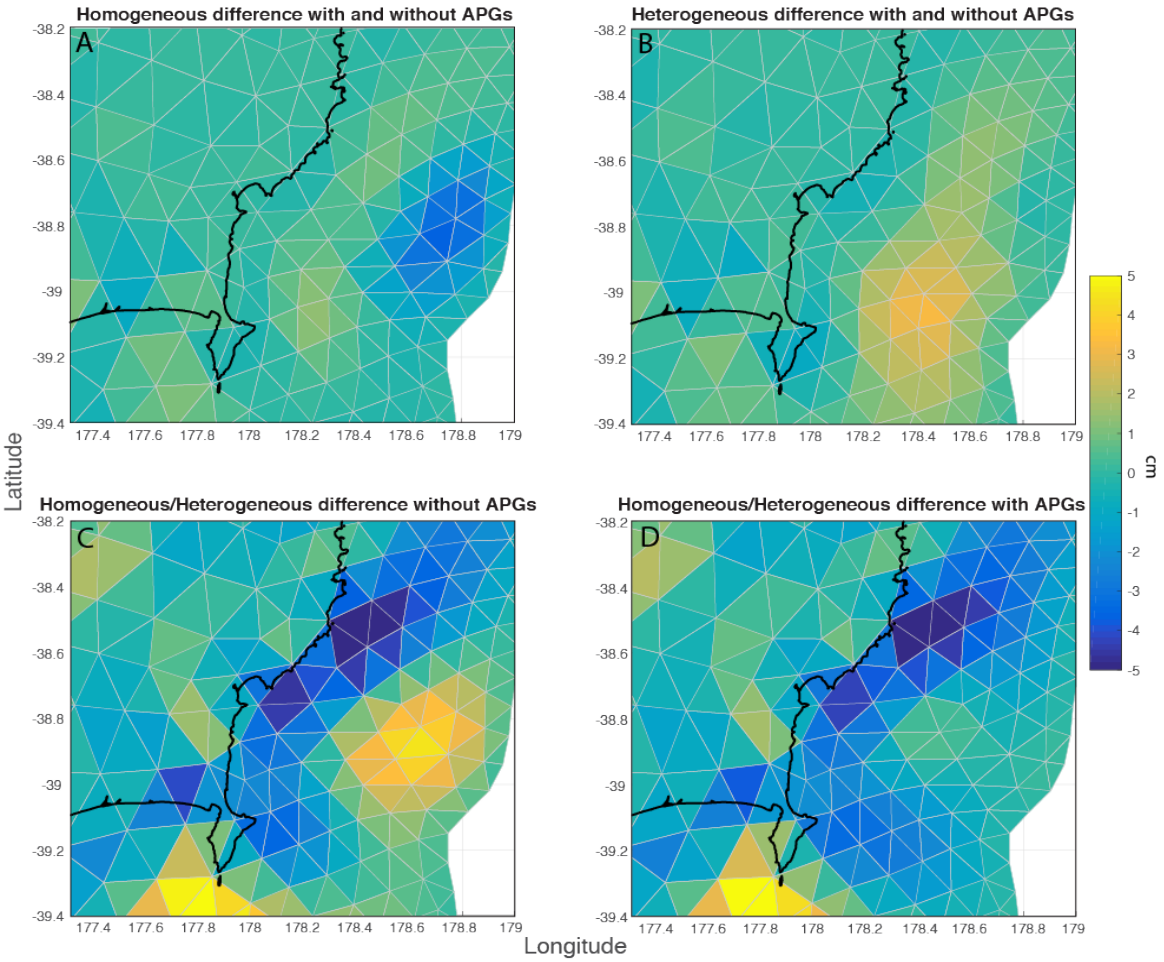

Figure 2.5: Differences between slip models. A) Difference between homogeneous models, B) difference between heterogeneous models, C) difference between models without APGs, and D) difference between models with APGs.

It's important to note where the two estimates of the location of the 1947 March 25th tsunami earthquake provided by New Zealand's GeoNet fall in relation to the slip distribution (**Figure 2.4**). The more northward estimate falls right outside of the peak slip amplitude for both of the homogenous cases, but appears to fall within the peak amplitude patch for both the heterogeneous cases. The more southward estimate falls along the edge of the entire slip patch in all four cases depicted. However, the heterogeneous elastic properties allow for more slip in that area than the homogeneous

case. But, unfortunately, the estimates of where these earthquakes actually occurred are subject to large errors due to lack of station coverage in 1947.

Figure 2.6 shows the formal error on total slip during the time period of the Gisborne SSE. Row A and row B show model runs with and without APGs using the same elastic properties. In the inversions without the APGs, the resolution is poor offshore where there are no stations and to the west where the plate interface is deepening. The tapering of error along the mesh boundaries is a result of assuming the slip and its error to be 0 just outside the mesh boundary. The third column in each row shows the difference between the first and second columns. For rows A and B, this allows a comparison between uncertainties with and without APGs. For the homogeneous case, I see that the inclusion of the APG data in the NIF inversion decreases the slip uncertainty directly below where they are placed by up to 1.79 cm. For the heterogeneous case, the number rises to 1.87 cm.

When comparing the uncertainties between similar models (whether with or without APGs) and only focusing on the type of elastic properties, as in rows C and D, its apparent that the uncertainties for the homogeneous case are less than the heterogeneous case. This is likely because of the added complexity of using varying elastic properties along the slip interface, which introduces tradeoffs between slip locations. However, when comparing the two, it's clear that the main source of varying uncertainty is offshore where the model resolution is poor to begin with. So, although the inclusion of APGs decreased the error more in the heterogeneous case, the uncertainties are still higher than the homogeneous case. These uncertainties do not take into account any uncertainty in the elastic properties themselves, and assume the elastic properties are perfectly known.

As the heterogeneous Green's functions represent more physically accurate elastic properties, this model is assumed to be more accurate despite the higher uncertainties. In fact, the uncertainties associated with the heterogeneous models represent a better estimate of true model uncertainty than the homogenous model uncertainties.

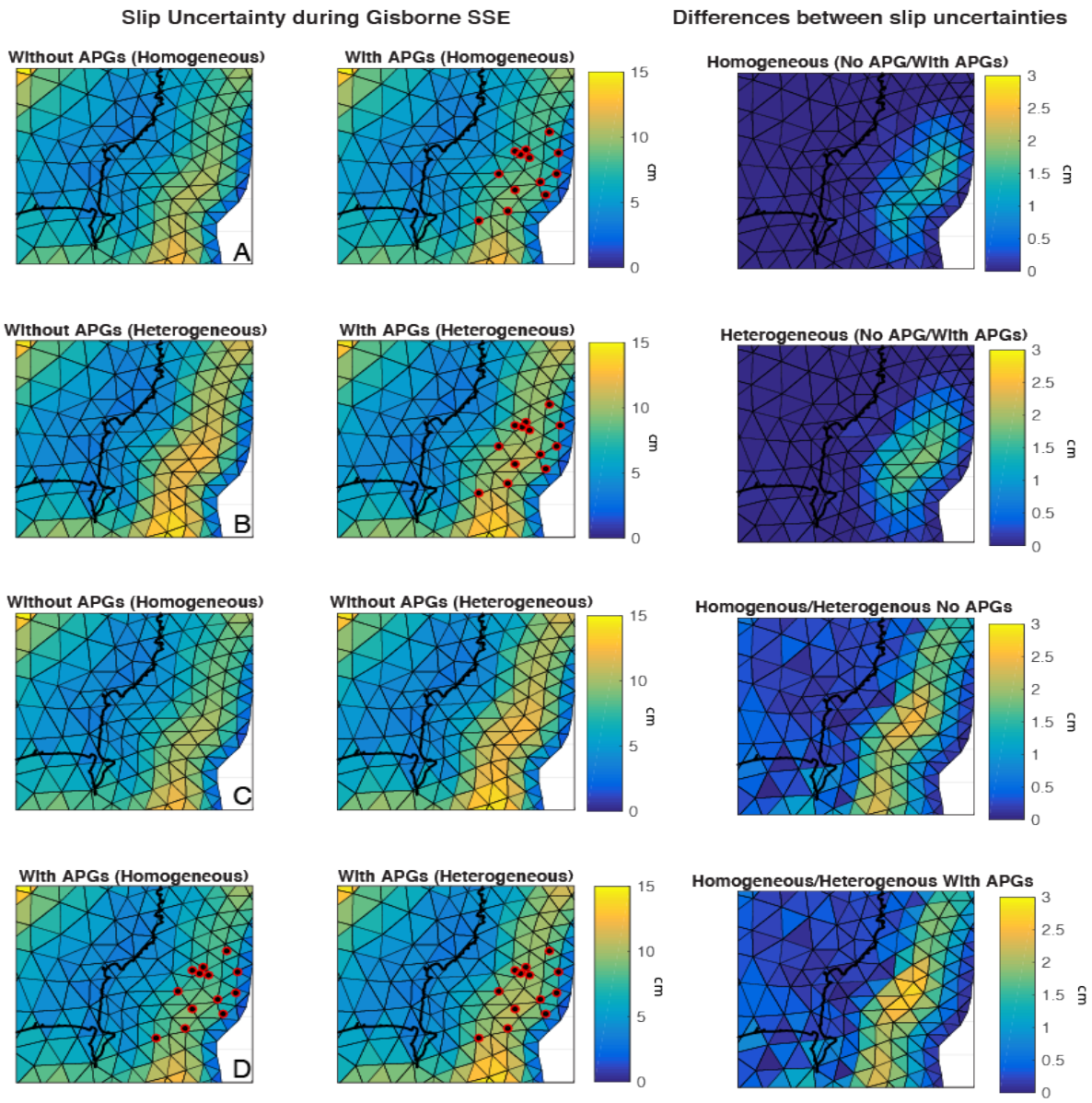

Figure 2.6: Formal slip error estimates. Row A) error estimates for homogeneous runs, B) error estimates for heterogeneous runs, C) error estimates between models without APGs, and D) error estimates for models with APGs. APG locations are highlighted as red circles.

Figures 2.7 and **Figure 2.8** show the model fits to solely GPS (**2.7**) and cGPS + APGs (**2.8**). Among the GPS stations in all four inversions, there is no obvious differences among the model fits, although collectively there is enough to change the total slip amplitudes. There is, however, considerable differences among APG fits. In the homogeneous inversions (column A, **Figure 2.8**), the transient is much more prominent in nearly every station. This is a likely cause of the extra slip. In some stations, such as SBP1, the model over predicts the displacements. When comparing the transients themselves, they appear considerably broader than the transients on the GPS stations. These figures also show how noisy the APG data really is when compared to GPS. Note that there is subsidence in all the stations before the transient. Whether or not that is a real signal, or is oceanographic or other noise, is not well constrained.

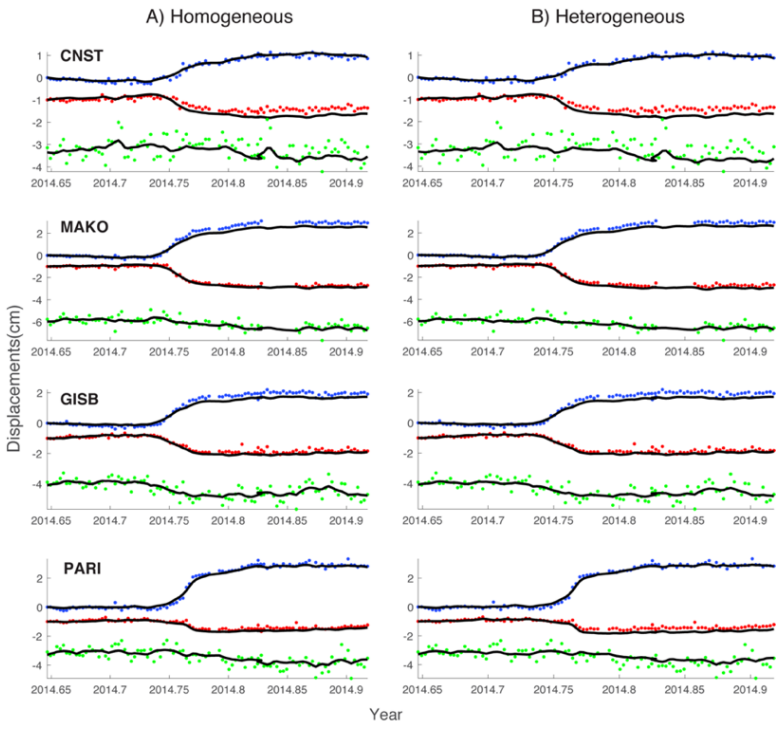

Figure 2.7: Model fits to cGPS data for cGPS inversions only.

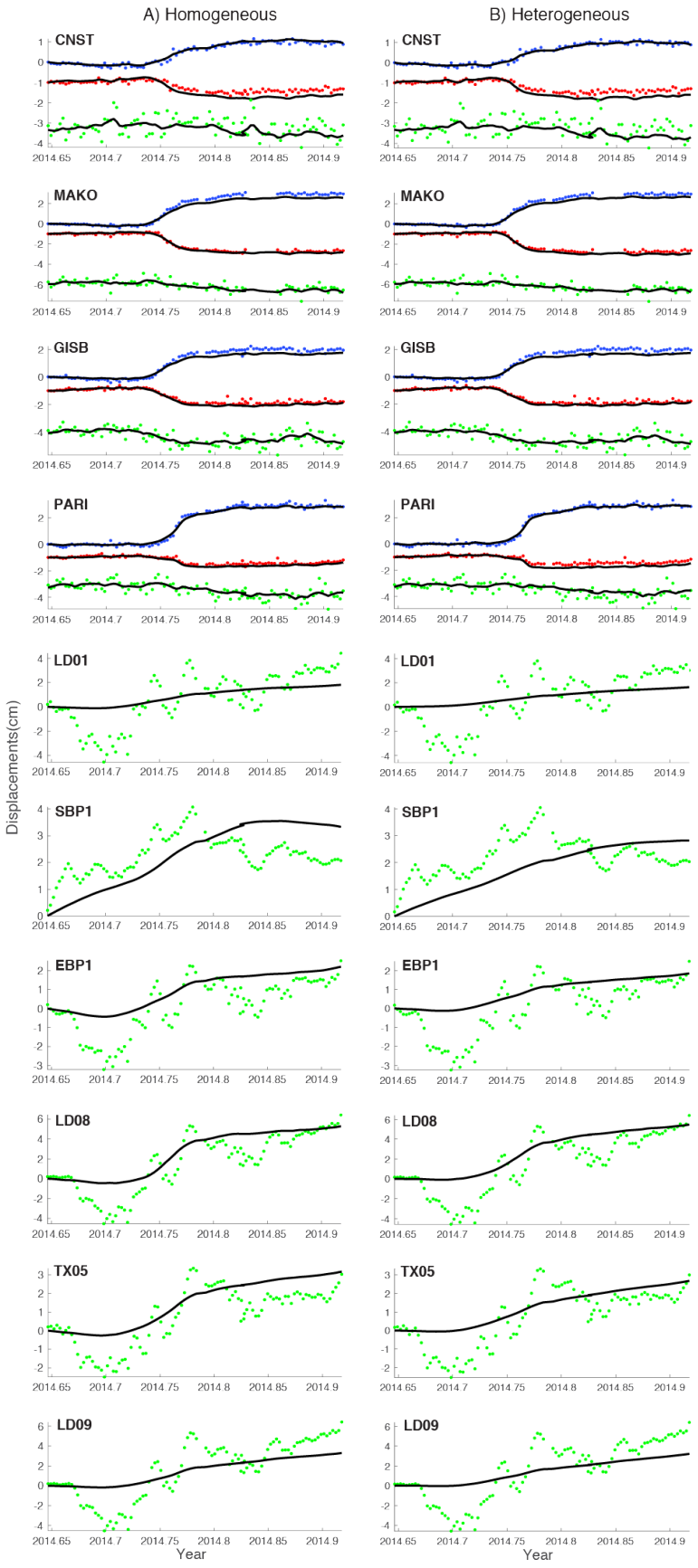

Figure 2.8: Model fits to data for co-inversions of cGPS and APG for homogeneous (A) and heterogeneous (B) elastic properties. E – Blue, N – Red, U – Green. Note that APGs (LD01, SBP1, EBP1, LD08, TX05, and LD09) only have vertical components.

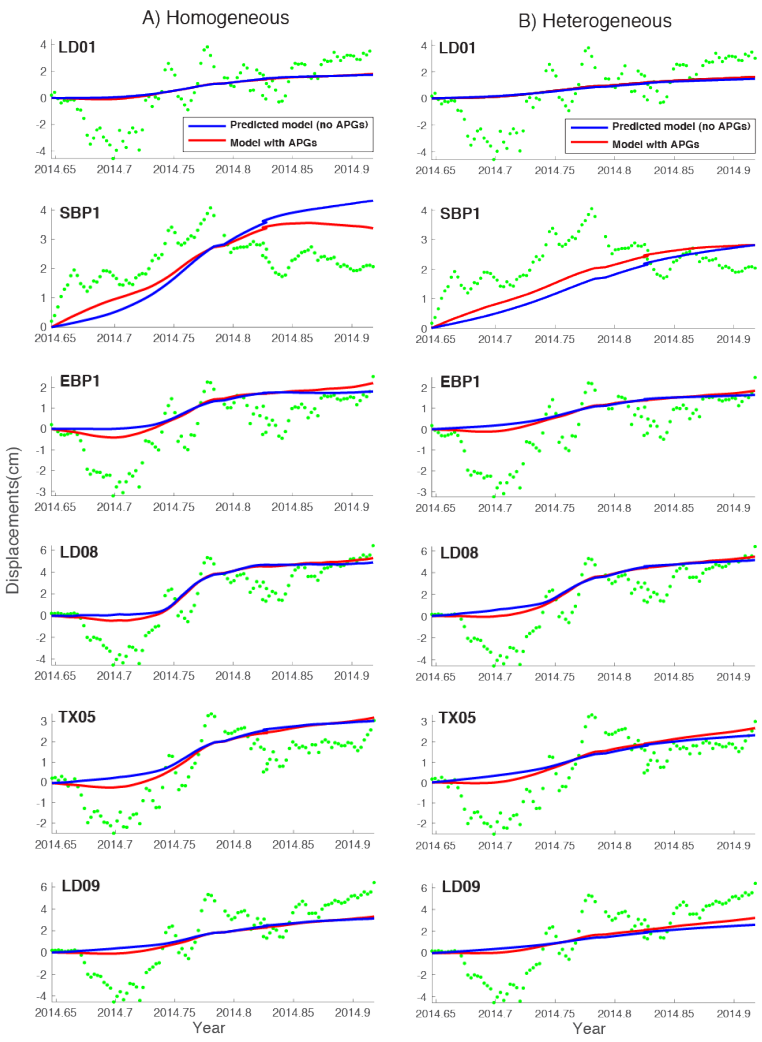

Figure 2.9: Predicted model fits at APG sites for inversions without APGs (blue) and actual model fits to APGs (red).

Figure 2.9 show the predicted model fit to the APG station sites for the inversions without APGs (blue) compared to the model fit to the APG stations for inversions with APGs (red). For the majority of the stations, with the exception of the homogeneous SBP1, the model fits to the APG data are more than the predicted models. Additionally, the predicted models fail to capture the subsidence modeled by the APGs around 7/2014.

Figures 2.10 and **2.11** show snapshots of 5-day averages of slip-rate between 9/14/2014 – 10/24/2014 without and with the APG data (A and B, respectively), using homogeneous (**2.10**) and heterogeneous (**2.11**) elastic properties. The increase in total slip

amplitude described in **Figure 2.4** for the inversions with APGs included is consistent across each time period. The inclusion of the APG data does not change the location of the peak slip amplitude, however, the slip distribution becomes broader with slip extending further updip at earlier time periods for the heterogeneous case.

Additionally, the model including the APG data suggests that the onset of the SSE is several days earlier than the cGPS-only inversion indicates. **Figures 2.10** and **2.11A** shows that when considering only cGPS data, the SSE begins between 9/29-10/4 while including the APG data suggests an onset closer to 9/24. This is likely a function of the subsidence mentioned in **Figures 2.7, 2.8,** and **2.9**, which is in turn a function of the values of the random walk amplitude and reference frame correction variance assigned to the APG data; larger random walk amplitudes and reference frame variances reduce this effect because the NIF is able to fit more of the APG data as random walk noise or reference frame correction. The earlier onset is clearer in the heterogeneous case compared to the homogenous models.

When comparing the homogeneous case with the heterogeneous one, the major difference is the SSE propagation. In the homogeneous case, the slip is more evenly distributed among the entire slip patch for inversions both with and without APGs, specifically between 9/29 – 10/14. Although the peak slip amplitude does migrate downdip and southward between 9/29 – 10/9 before slipping along the whole patch equally between 10/9-10/14 **(Figure 2.10**).

The heterogeneous case has a more pronounced slip migration, and the differences between inversions with and without APGs are clearer (**Figure 2.11**). For the heterogeneous case, the peak slip on 9/29 starts along the shore, where the homogeneous

starts offshore. This peak amplitude in the heterogeneous case then moves slightly offshore and to the south through 10/14, whereas the homogeneous case has a more broadly distributed slip path during this entire time.

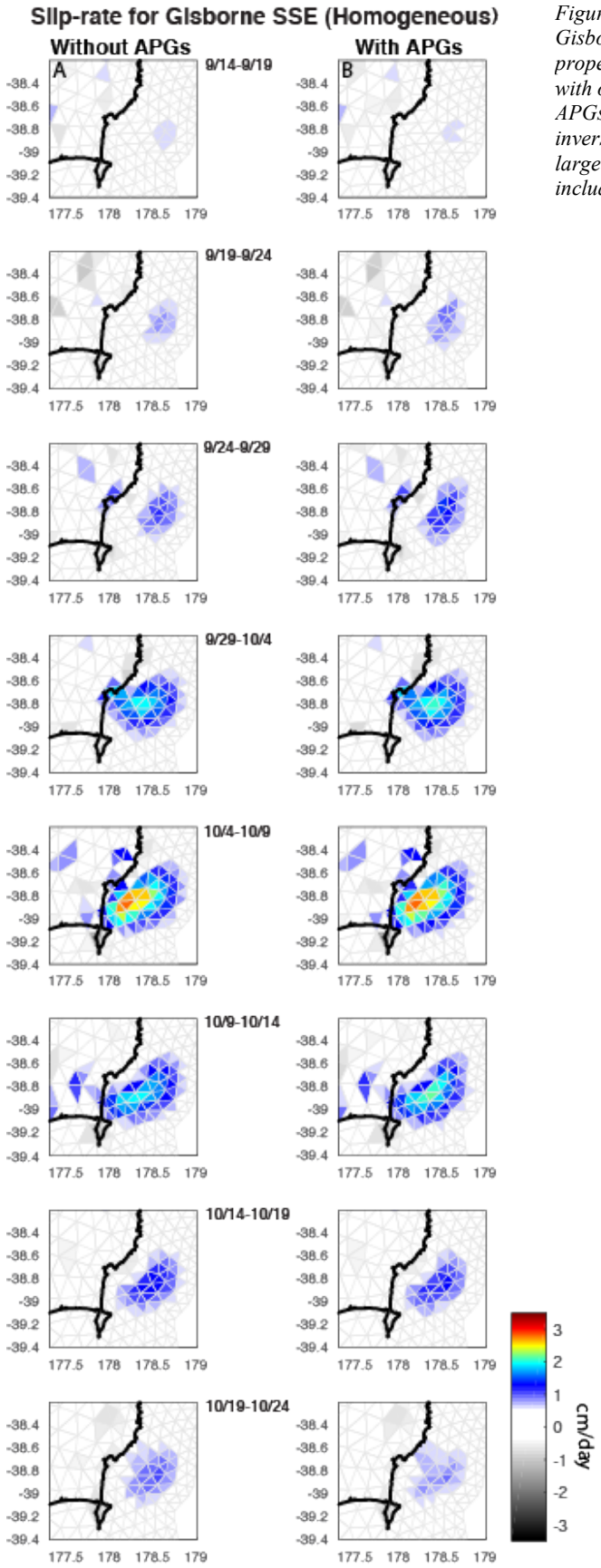

Figure 2.10: Time-dependent model of Gisborne SSE using homogeneous elastic properties. Column A shows the inversion with only GPS while B shows it with GPS and APGs. When the APGs are added to the inversion, it appears that the SSE intensity is larger during the early part of the SSE. This includes an apparent early onset time.

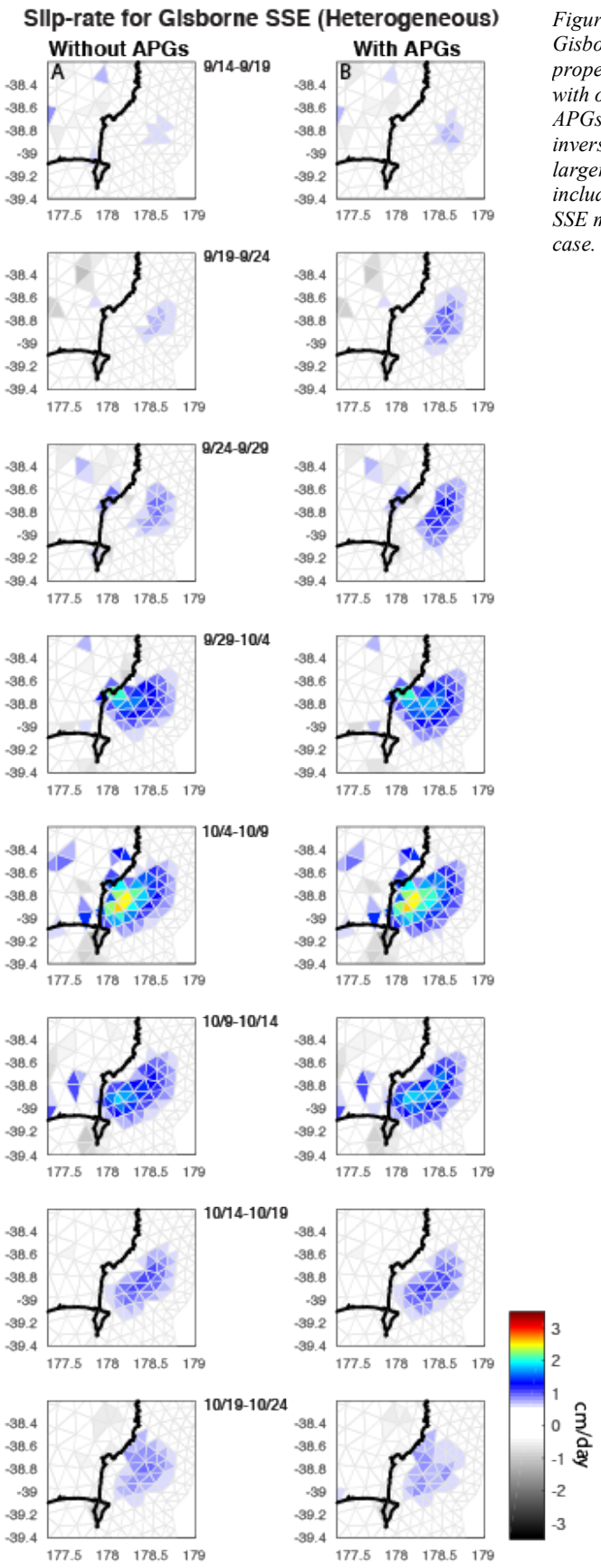

Figure 2.11: Time-dependent model of Gisborne SSE using heterogeneous elastic properties. Column A shows the inversion with only GPS while B shows it with GPS and APGs. When the APGs are added to the inversion, it appears that the SSE intensity is larger during the duration of the SSE. This includes an apparent early onset time. The SSE migration is clearer in the heterogeneous case.

CHAPTER 3:

STATIC MODELS:

MOMENT BOUNDING

3.1 Moment Bounding Methods

Seismic moment has become a useful way to measure earthquake size and energy and underlying fault properties. As a scalar value, it describes total energy released by fault slip (**equation 3**). In this case, fault area and slip can be summed over multiple subfault patches, i.e the mesh used in the NIF inversions, to yield a total seismic moment. It is possible to rigorously bound the minimum and maximum seismic moment released during a slow slip event using constrained least squares inversions, which I will denote as the moment bounding method (*Johnson et al. 1994*, *Murray & Segall 2001*, and *Maurer et al. 2017*). In the moment bounding method, this range of least squares inversions solves for plate interface slip during the 2014 Gisborne SSE and is constrained by varying values of seismic moment, which is fixed for each inversion. This allows for exploration of the variety of models that fit the data within plausible limits.

This method can be a powerful tool to better understand model uncertainty as the NIF produces a single model for each set of inputs but does not give an indication of the range of slip distributions that could fit the data. By having a range of possibilities, it's possible to understand the uncertainties and constraints on the slow slip region. This has implications for long term slip budgets, which is important for forecasting potential seismic hazards and how much slip is available for future earthquakes. Additionally, since slow slip can be helpful when determining where locked and unlocked regions of a subduction zone are, having a variety of slip models that fit the data can help estimate where the locked patches are.

I am interested in the total seismic moment, defined as,

$$M_o = \mu \iint_A s \, dA \tag{3}$$

where μ is the shear modulus (ratio of shear stress to shear strain), A is the fault area that slipped, and s is the spatially variable amount of slip. Because I used a mesh of triangular subfaults, the integral in **equation 3** is approximated as a sum of slip times the area for each triangular subfault.

For this inversion, I minimize the following:

$$\frac{min}{x} \frac{1}{2} \|Gs - d\|_2^2 \; such \; that \begin{cases} \mu \sum As = M_o \\ lb \leq s \leq ub \end{cases} \tag{4}$$

where G is the Green's Function matrix, s is the slip vector (strike and dip-slip components for each triangle patch in the mesh) I am solving for, d is the displacements of the cGPS and APG stations during the SSE (taken from *Wallace et al. 2016*), A is the area of each triangular fault patch, μ is the shear modulus, M_o is SSE moment, *lb* is the lower bound placed on the slip vector, and *ub* is the upper bound. The Green's Functions are the same as used in the NIF. The mesh was also modified to remove poorly resolved, far away fault patches. The lower bound was set to 0 cm (essentially a non-negative slip constraint) where the upper bound was set to a conservative 42 cm (assuming a 10-year repeat interval at a plate rate of 44 mm/yr). This process is repeated at a number of values of M_o, obtaining the best fitting slip distribution with a given seismic moment.

This produces a suite of slip distributions at a range of moments. I consider 10,000 separate moment values extending from $9.5545\ x\ 10^{16} Nm$ to $3.8218\ x\ 10^{20} Nm$ assuming a shear modulus of 30MPa. An initial moment was calculated by using **equation 3** and assuming uniform slip (1m of slip for each triangular subfault). A range was thus picked though iterations that captured the misfit curve shape (**Figure 3.1**).

Each moment value will produce a slip distribution. This slip distribution will be multiplied by the original Green's functions to produce predicted GPS and APG displacements (**equation 2**). The misfit between the observed GPS/APG response and the predicted GPS/APG response will give us our best fit and range for possible moments that fit the original data. Misfit ($\emptyset_M$) as a function of moment is defined by:

$$\emptyset_M = Norm(\frac{r^2}{\sigma}) \tag{5}$$

where r is the residual between the predicted and observed data, σ is a covariance matrix and Norm indicates the L2 norm. After each set of moments, a 'misfit curve' is produced similar to those of *Murray and Segall 2001*.

Following *Maurer et al 2017*, I took the misfit curve and created a normalized probability density function (PDF) for the probability of each slip inversion for a given seismic moment. The PDF is defined as:

$$P = e^{-\frac{1}{2}\emptyset_M} \tag{6}$$

By taking the PDF and turning it into a cumulative density function (CDF), a credible interval (CI) can used to create our upper and lower bounds of acceptable slip ranges. A 95% credible interval corresponds to models between 2.5% and 97.5% on the CDF. The justification in doing this, instead of using the minimum of the misfit curve, comes from *Mauer et al 2017*. The original papers on this process, *Johnson et al 1994, Murray and Segall*, *Murray and Johnson 2014* used the minimum of the misfit curve as their best-fit scenario, while also using bootstrapping, L1 norms, or Chi-Squared methods method to classify confidence intervals. *Maurer et al. 2017* tested each of these methods and found that by turning the standard misfit curve into a PDF and using a CDF for credible intervals, this method reduces uncertainties when assuming that interseismic slip is everywhere bounded between locked and creeping. Since no locking constraints have been incorporated, it is assumed that this method will provide conservative bounds on the moment values and slip models. I performed two different sets of moment bounding inversions; one including APGs and one without.

3.2 'Moment Bounding' Results

Figure 17 shows the misfit (cm) versus moment (Nm) (**A**) and the associated probability density functions from **equation 4** (**B**) for homogeneous elastic properties without APGs (yellow) and with APGs (green) and heterogeneous elastic properties without APGs (blue) and with APGs (red). There are several differences in the model misfits between the for different model runs. First, when comparing the misfit curves between homogeneous and heterogeneous elastic properties, we see the misfits for inversions with homogeneous properties climb more rapidly for the range of moments than the heterogeneous counterpart. This is likely due to the same reasons discussed in

Figure 2.3. In both cases, the runs including APGs have a steeper slope than without the APGs. This makes sense, since there is more data. However, because of this, there is better resolution offshore, and the resulting probability density function for the inversions with APGs involve a sharper maximum and narrow down the acceptable moments.

Figures 3.2 (homogeneous) and **3.3** (heterogeneous) show the CDF's (A) with 95% credible intervals labeled as dashed lines. B/C, D/E, F/G show the lower bound, best fitting, and upper bound taken for models without APGs and with APGs, respectively. The values are summarized in **Table 3.1**.

Because the PDF was 'tighter' in the APG-included inversions, this decreased the difference in lower and upper bounds. For the homogeneous cGPS only, the lower bound was $4.387\ x\ 10^{18} Nm$ and the upper bound was $1.855\ x\ 10^{20} Nm$. With the APGs, that range is lowered to $5.166\ x\ 10^{18} Nm$ and the upper bound was $1.849\ x\ 10^{20} Nm$. The heterogeneous models had a similar result. In all cases but the upper bounds for the different elastic properties, the inclusion of the APGs increased the moment.

The range of moments and resulting slipping regions that can fit the data are wide, especially on the upper end. For homogeneous cGPS only inversions peak slip for the lower bound, best fit, and upper bound are 20.48 cm, 26.13 cm, and 42.00 cm, respectively. For homogeneous cGPS + APGs, those values are 26.38 cm, 23.45 cm, and 42.00 cm. For heterogeneous cGPS only inversions peak slip for the lower bound, best fit, and upper bound are 17.63 cm, 33.62 cm, and 42.00 cm, respectively. For heterogeneous cGPS + APGs, those values are 27.63 cm, 29.61 cm, and 42.00 cm. Using these values, it's apparent that the best-fitting model from this method roughly captures roughly what the peak amplitude is from the NIF models. However, in both the

homogeneous and heterogeneous models, including APGs lowers these peak slip values. The heterogeneous cGPS only inversion has a considerably high peak slip value compared to the other models. For both the homogeneous and heterogeneous lower bound models with APGs, peak slip is comparable to the NIF results as well as the best fitting moment bounding models, although it is concentrated on only a few triangular patches (**3.2, 3.3**). The upper bound maxes out at 42 cm for all cases.

When comparing moment values between the NIF (**table 2.1**) and moment bounding (**table 3.1**), we see that the best fitting models for the heterogeneous cases are relatively similar (NIF: cGPS - 2.32 x 10^{19} Nm, cGPS + APG - 2.58 x 10^{19} Nm & Moment Bounding: cGPS – 2.931 x 10^{19} Nm, cGPS + APG – 2.58 x 10^{19} Nm). The homogeneous models are not as close (NIF: cGPS - 2.13 x 10^{19} Nm, cGPS + APG - 2.058 x 10^{19} Nm & Moment Bounding: cGPS – 1.179 x 10^{19} Nm, cGPS + APG – 1.627 x 10^{19} Nm), but still show within the same order of magnitude and error. Although the moment bounding homogeneous case doesn't match as well with the NIF, the best fitting moment model for cGPS + APG is nearly exact what Wallace et al. 2016 produced (1.60 x 10^{19} Nm and peak slip ~23 cm). Similarly, the moment values and peak slip for the heterogeneous cGPS + APG case is are consistent with *Williams and Wallace 2018.*

The addition of the APGs has a more telling difference in where the highest residuals come from and how the slip is accommodated. By comparing **Figure 3.2** and **Figure 3.3**, at a first-order look, the GPS fits seem to be highly comparable between the two. At the lower boundary (B/C), the cGPS only model fits the data relatively well by moving the slip patch downdip and underneath the easternmost stations. However, the added constraint of the APGs causes much larger residuals in the GPS in order to keep

the slip patch offshore as well as the moment consistent. At the higher boundary (F/G), slip is accommodated by creating large slipping patches in the deepest part of the mesh, as well as putting slip far away offshore. For the cGPS models, doing this allows the model to fit the GPS decently well, because larger slipping patches farther away from stations will not affect GPS stations as much. The APGs once again constrain the slip, forcing more slip downdip and reducing slip directly below the APG stations and southward. This is the cause of the lower moment with the addition of the APGs. In addition to constraining the amplitude of slip on these patches, the spatial distribution for the APG-included inversions is much coarser than the inversions without. Finally, even at the upper boundary, the addition of the APGs prevent the model from including slip everywhere in the near trench region at the maximum allowable amount, as in the GPS only upper bound. This indicates that the APGs do not allow for the SSE to fully rupture to the trench and that some of the plate interface near the trench is likely locked.

Table 3.1 Summary of moment bounding misfit and slip values for best fit and minimum/maximum ranges within the 95% confidence interval.

Model	Peak Slip (cm)	Seismic potency (m^3)/ seismic moment (Nm)
Homogeneous		
MB Best-fit: cGPS	26.13	1.179 x 10^{19}
MB Best-fit: cGPS + APGs	23.45	1.627 x 10^{19}
MB Lower Bound: cGPS	20.48	4.387 x 10^{18}
MB Lower Bound: cGPS + APGs	26.38	5.166 x 10^{18}
MB Upper Bound: cGPS	42.00	1.855 x 10^{20}
MB Upper Bound: cGPS + APGs	42.00	1.849 x 10^{20}
Heterogeneous		
MB Best-fit: cGPS	33.62	2.931 x 10^{19}
MB Best-fit: cGPS + APGs	29.61	2.503 x 10^{19}
MB Lower Bound: cGPS	17.63	4.776 x 10^{18}
MB Lower Bound: cGPS + APGs	27.63	5.150 x 10^{18}
MB Upper Bound: cGPS	42.00	1.873 x 10^{20}
MB Upper Bound: cGPS + APGs	42.00	1.869 x 10^{20}

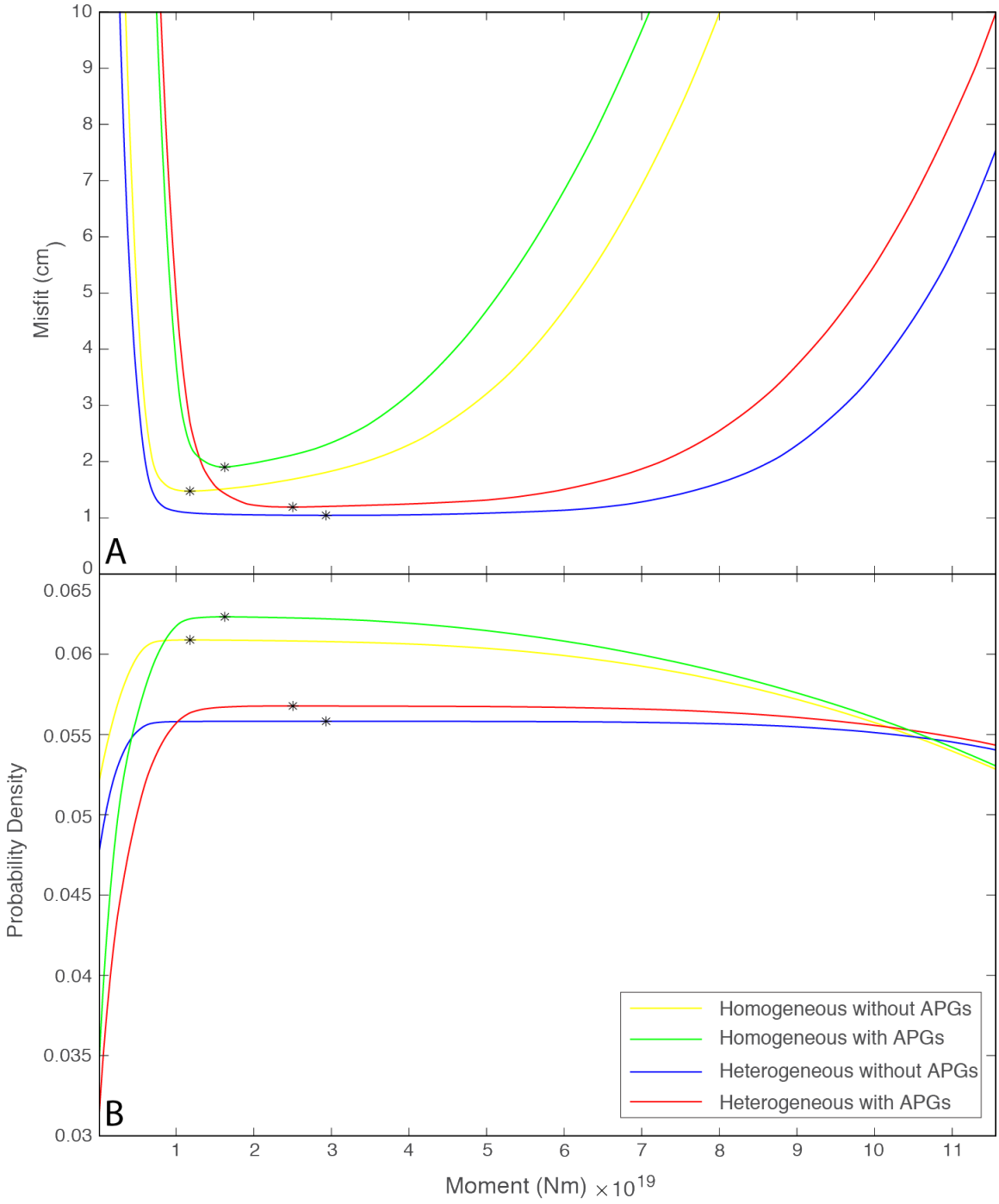

*Figure 3.1: Moment bounding results for homogeneous cGPS (yellow), homogeneous cGPS + APGs (green), heterogeneous cGPS (blue), and heterogeneous cGPS + APGs (red). A is the misfit vs seismic moment with minimum moment labeled as black *'s. B is the PDF vs moment, with maximum probabilities labeled as black *'s. Generally, the runs with APGs result in higher misfits (more data) but also narrow the range of moments. The heterogeneous realistic properties allow for higher moments as well.*

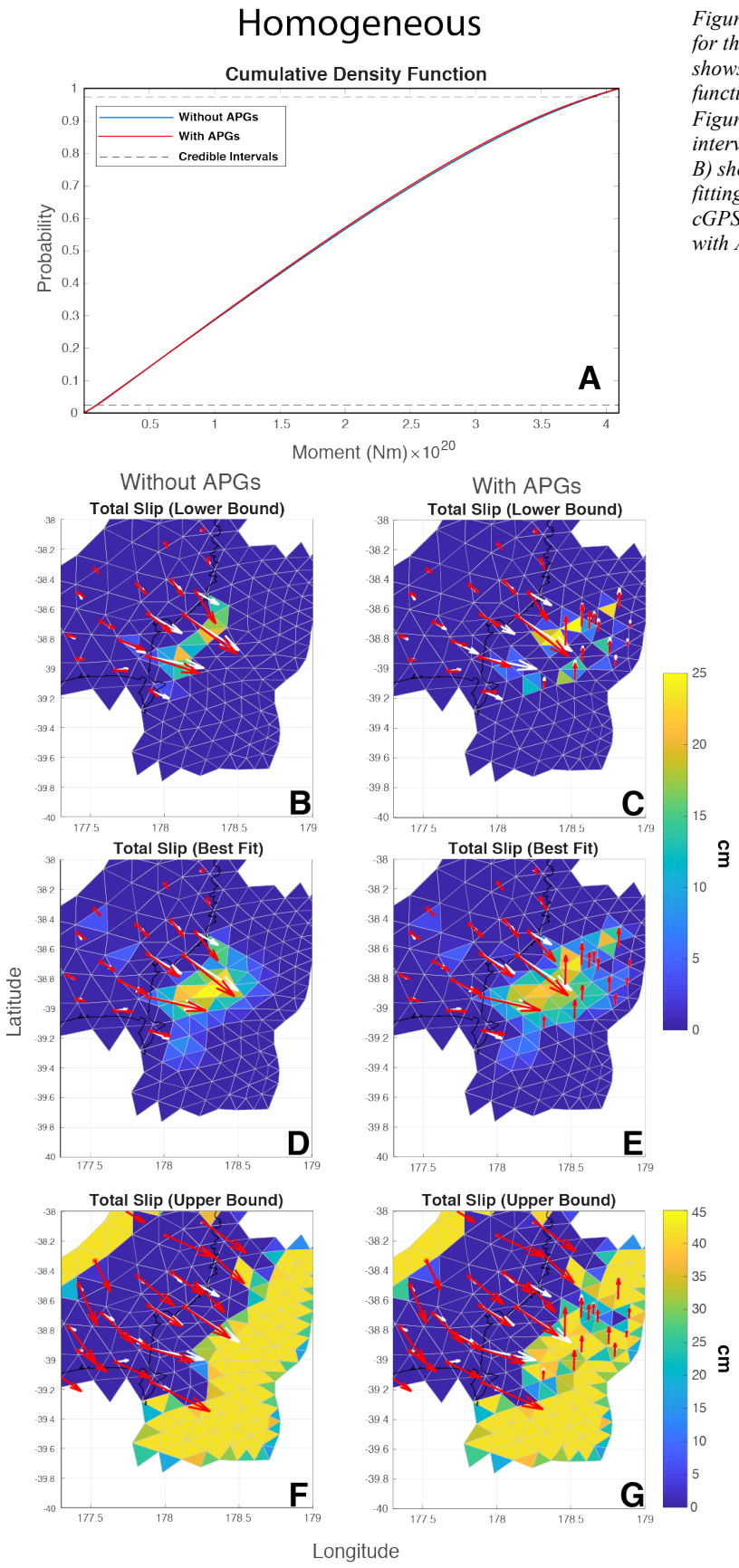

Figure 3.2: Moment bounding results for the homogeneous only case. A) shows the cumulative density function of the normalized PDF from Figure 17 with 95% credible intervals outlined with dashed lines. B) shows the lower bounds, best fitting mode, and upper bounds for cGPS only case. C is the same, but with APGs.

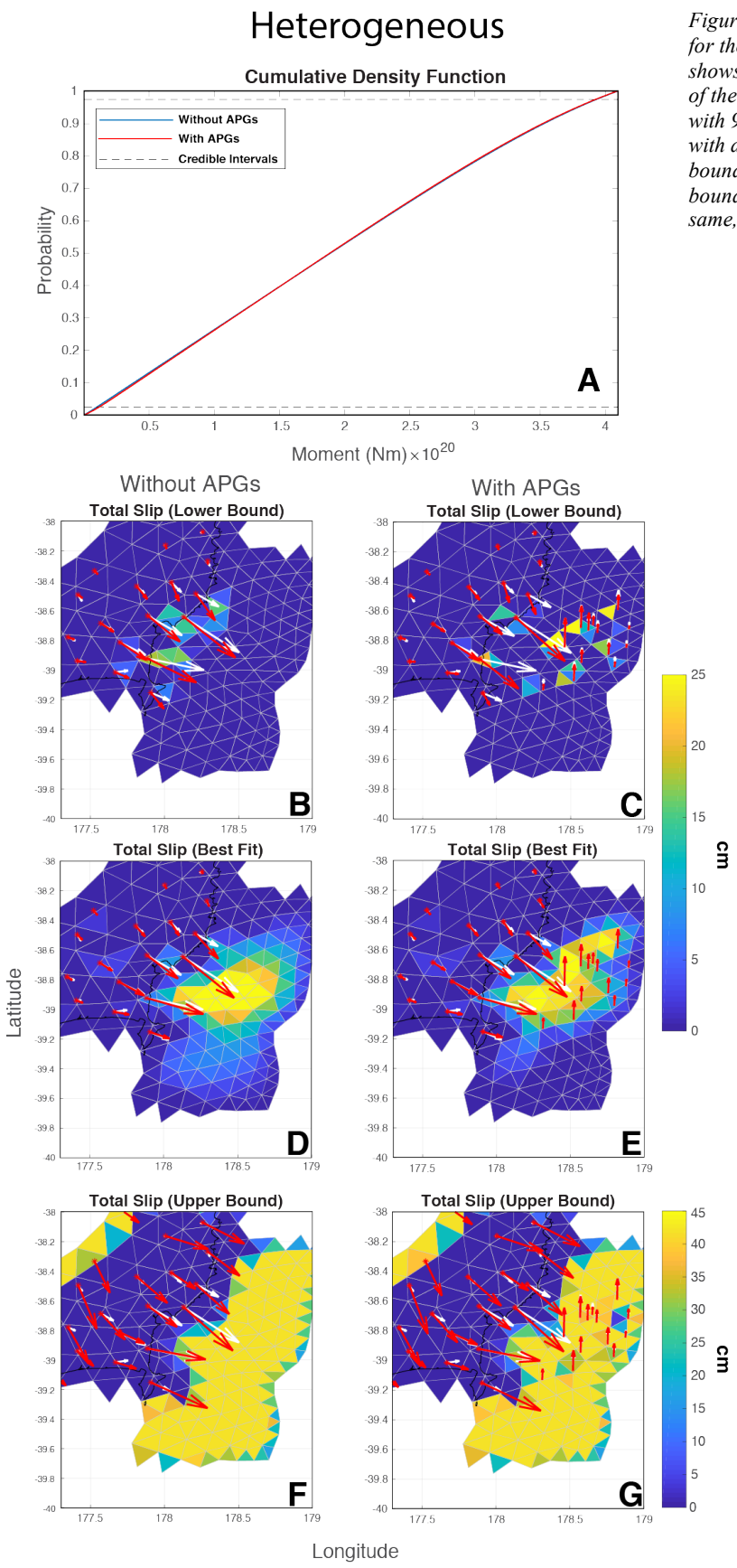

Figure 3.3: Moment bounding results for the heterogeneous only case. A) shows the cumulative density function of the normalized PDF from Figure 17 with 95% credible intervals outlined with dashed lines. B) shows the lower bounds, best fitting mode, and upper bounds for cGPS only case. C is the same, but with APGs.

CHAPTER 4:

CONCLUSIONS

As the years go on, and as we continue to learn more about SSEs, both onshore and off, it will be crucial to justify the addition of more stations. As SSEs have already been established as being connected to devastating earthquakes, it must be shown that adding more data can help resolve areas with poor resolution. One of the most crucial areas for hazards, and the area most poorly resolved by conventional onshore cGPS networks, is the offshore near trench region.

As seen in **Figure 1.4** and **Figure 2.1**, signal to noise ratio in APGs is a major problem for our current offshore pressure gauge data. This is also demonstrated by the model fits shown in **Figures 2.7** and **2.8.** The SSE transient is more difficult to pick out of the APGs than the GPS. Not only is the transient more 'broad', but there appears to be subsidence occurring before the SSE. Whether this subsidence is interpreted as real signal or noise has a large impact on the onset timing of the 2014 Gisborne SSE. It is telling that the cGPS only models are completely unable to predict this subsidence (**Figure 2.9**).

These results show that while our current APG data is useful for increasing resolution of slip location and timing offshore (**Figure 2.6**), the high level of noise in these data relative to cGPS makes interpretation and modeling difficult. Decreasing the APG noise by, for example, learning to better correct remaining oceanographic noise signals will be crucial for advancing our understanding of deformation in offshore regions in future studies.

Additionally, as the complexity of geodetic models continues to increase, it's important to be able to say something about what increasing complexity does our models and their uncertainties. Added complexity in this study includes both added APG stations in areas of poor resolution, as well as realistic elastic properties. As this study has shown,

more instrumentation can significantly decrease the uncertainties in offshore regions. However, this uncertainty decrease is confined to be directly underneath the instruments themselves. Having stations running along the entire trench with increased signal to noise ratios would be the only way to get the model resolution to be as good as on land.

Since this is the first time-dependent study of an offshore slow slip event coupled with realistic heterogeneous Green's Functions, we now have the most detailed view of one of these events. And more importantly, the location of this study is near to known tsunami earthquakes. The results of this study may be used to better constrain the overall slip budget and future earthquake potential of this region.

As *Kato et al. 2012* observed, the 2011 Tohoku-Oki earthquake was preceded by a slow-slip event leading to the hypocenter. If we look at the models that could be produced before this study, i.e. the homogeneous case without APGs (**Figure 2.10A),** the migration patterns of the SSE are much different than the more realistic case with heterogeneous elastic properties and APGs (**Figure 2.11B**). In the homogeneous, no APG case, the slip patterns are confined to a single area and are more spread out. In the heterogeneous, APGs included case, the migration pattern shows three real migrations of peak slip (between the panels shown). This migration pattern moves from N to S then spreads out in between. If you take the more northern 1947 March earthquake location estimate, speculation can be made that a similarly migrating SSE could have caused stress release leading up to the earthquake. Unfortunately, the earthquake location estimates are highly uncertain and do not include any geodetic data, so we cannot draw firm conclusions about the possible role of any SSE in triggering these tsunami earthquakes.

The addition of the APGs also provide better estimates of upper and lower bounds on moment release estimates for a static inversion case. Although the upper bounds of both cases show a very unlikely scenario, it does showcase that the addition of the APG data can significantly narrow uncertainty bounds on estimated slow slip moment while demonstrating that even in unrealistic circumstances, slip is removed away from the subduction zone trench, suggesting that this area is locked.

References

Bartlow, N. M., L. M. Wallace, R. J. Beavan, S. Bannister, and P. Segall (2014). Time-dependent modeling of slow slip events and associated seismicity and tremor at the Hikurangi subduction zone, New Zealand. *J. Geophys. Res.*

Bassett, D., Sutherland, R., Henrys, S., Stern, T., Scherwath, M., Benson, A., Toulmin, S., Henderson, M. (2010), Three dimensional velocity structure of the northern Hikurangi margin, Raukumara, New Zealand: Implications for the growth of continental crust by subduction erosion and tectonic underplating. *Geochemistry Geophysics Geosystems*, 11(Q10013).

Brudzinski, M. R., & Allen, R. M. (2007). Segmentation in episodic tremor and slip all along Cascadia. *Geology,35*(10), 907-910.

Cayol, V., & Cornet, F. H. (1998), Effects of topography on the interpretation of the deformation field of prominent volcanoes application to ETNA. *Geophysical Research Letters*, 25, 1979–1982.

Dragert, H., K. Wang, and T. James (2001), A silent slip event on the deeper Cascadia subduction interface, *Science*, 292, 1525–1528.

Eberhart-Phillips, D., Reyners, M., Bannister, S., Chadwick, M., Ellis, S. (2010), Establishing a versatile 3-D seismic velocity model for New Zealand. *Seismological Research Letters*, 81(6), 992–1000.

Eberhart-Phillips, D., &Reyners, M. (2012), Imaging the Hikurangi plate interface region with improved local-earthquake tomography. *Geophysical Journal International*, 190, 1221–1242.

Eberhart-Phillips, D., and Bannister, S. (2015), 3-D Imaging of the northern Hikurangi subduction zone, New Zealand: variations in subducted sediment, slab fluids and slow slip. *Geophysical Journal International*, 201(2), 838-855,

Fujie, G., Miura, S., Kodaira, S., Kaneda, Y., Shinohara, M., Mochizuki, K., Kanazawa, T., Murai, Y., Hino, R., Sato, T., Uehira, K. (2013). Along-trench structural variation and seismic coupling in the northern Japan subduction zone. *Earth, Planets and Space,65*(2), 75-83.

Ito, Y., Hino, R., Kido, M., Fujimoto, H., Osada, Y., Inazu, D., Ohta, Y., Linuma, T., Ohzono, M., Miura, S., Mishina, M., Suzuki, K., Tsuji, T., Ashi, J. (2013). Episodic slow slip events in the Japan subduction zone before the 2011 Tohoku -Oki earthquake. *Tectonophysics,600*, 14-26.

Johnson, H. O., Agnew, D. C. & Hudnut, K. Extremal bounds on earthquake movement from geodetic data: Application to the Landers earthquake. *Bull. Seismol. Soc. Am.* 84, 660-667 (1994)

Koulali, A., Mcclusky, S., Wallace, L., Allgeyer, S., Tregoning, P., Danastasio, E., & Benavente, R. (2017). Slow slip events and the 2016 Te Araroa M w 7.1 earthquake interaction: Northern Hikurangi subduction, New Zealand. *Geophysical Research Letters,44*(16), 8336-8344.

Larson, K., A. Lowry, V. Kostoglodov, W. Hutton, O. Sanchez, K. Hudnut, and G. Suarez (2004), Crustal deformation measurements in Guerrero, Mexico, *J. Geophys. Res.*, 109(B4), B04409.

Maurer, J., & Segall, P., Bradley, AM., (2017) Bounding the moment deficit rate on crustal faults using geodetic data: Methods. *J. Geophys. Res.*, 122, 8, 6811-6835

McTigue, D., & Segall, P. (1988), Displacements and tilts from dip-slip faults and magma chambers beneath irregular surface topography. *Geophysical Research Letters*, 15, 601–604.

Murray, Jessica, and Paul Segall. "Testing time-predictable earthquake recurrence by direct measurement of strain accumulation and release." *Nature* 419.6904 (2002): 287-91.

Obara, K., H. Hirose, F. Yamamizu, and K. Kasahara (2004), Episodic slow slip events accompanied by non-volcanic tremors in southwest Japan subduction zone, *Geophys. Res. Lett.*, 31, L23602,

Power, W., Wallace, L., Mueller, C., Henrys, S., Clark, K., Fry, B., Wang, X., Williams, C. (2016). Understanding the potential for tsunami generated by earthquakes on the southern Hikurangi subduction interface. *New Zealand Journal of Geology and Geophysics,59*(1), 70-85.

Segall, P., and M. Matthews (1997), Time dependent inversion of geodetic data, J. Geophys. Res., 102, 22,391–22,409.

Schmidt, D. A., & Gao, H. (2010). Source parameters and time-dependent slip distributions of slow slip events on the Cascadia subduction zone from 1998 to 2008. *Journal of Geophysical Research,115*(B4

Schwartz, S. Y., & Rokosky, J. M. (2007). Slow slip events and seismic tremor at circum-Pacific subduction zones. *Reviews of Geophysics,45*(3).

Wallace, L. M., & Beavan, J. (2010), Diverse slow slip behavior at the Hikurangi subduction margin, New Zealand. *Journal of Geophysical Research*, 115(B12402).

Wallace, L. M., Beavan, J., Bannister, S., Williams, C. (2012a), Simultaneous long-term and short-term slow slip events at the Hikurangi subduction margin, New Zealand: Implications for processes that control slow slip event occurrence, duration, and migration. *Journal of Geophysical Research*, 117(B11402)

Wallace, L. M., Barnes, P., Beavan, R. J., Van Dissen, R. J., Litchfield, N. J., Mountjoy, J., Langridge, R. M., Lamarche, G., Pondard N. (2012b), The kinematics of a transition from subduction to strike-slip: An example from the central New Zealand plate boundary. *Journal of Geophysical Research*, 117(B02405)

Wallace, L. M., Webb, S. C., Ito, Y., Mochizuki, K., Hino, R., Henrys, S., Schwartz, S. Y., Sheehan, A. F. (2016), Slow slip near the trench at the Hikurangi subduction zone, New Zealand. *Science* 352(6286), 701-704.

Williams, C. A., & Wadge, G. (1998), The effects of topography on magma chamber deformation models: application to Mt. Etna and radar interferometry. *Geophysical Research Letters*, 25, 1549–1552.

Williams, C. A., & Wadge, G. (2000), An accurate and efficient method for including the effects of topography in three-dimensional elastic models of ground deformation with applications to radar interferometry. *Journal of Geophysical Research Solid Earth*, 105(B4), 8103-8120.

Williams, C. A. and Wallace, L.M. (2018) The Impact of Realistic Elastic Properties on Inversions of Shallow Subduction Interface Slow Slip Events Using Seafloor Geodetic Data. *Geophysical Research Letters*. In Review.

Appendix – Publications

- Yohler, R., Bartlow, N., Wallace, L., Williams, C., Johnson, K. In prep. "Time Dependent Behavior of Near Trench Slow Slip Event Along Hikurangi Subduction Zone."

Appendix – Presentations

- Yohler, R., Bartlow, N., L., Williams, C., Johnson, K., 2017 "Constraining slip distributions and onset of shallow slow slip in New Zealand by joint inversions of onshore and offshore geodetic data." American Geophysical Union Conference. Poster. December 2017.
- Attended Southern California Earthquake Center Annual Conference September 2017
- Yohler, R., Bartlow, N., Wallace, L., Williams, C., 2017 "In the land of HOBITSS where the Slow Slip Events lie." EarthScope Annual Meeting. Poster. May 2017.

Appendix – Fellowships/Awards

- East Asia and Pacific Summer Institutes (New Zealand) Fellowship (2017)
- EarthScope Annual Meeting student scholarship (2017)
- Graduate Professional Council travel award (2017)

Appendix – Teaching/Professional Development

- Teaching Assistant, GEOL-G 1100 Principles of Geology, Department of Geological Sciences, University of Missouri (Fall 2017)
- American Association for Petroleum Geologist: President (2017)
- American Geophysical Union Member (2017)
- Volunteer: Dinosaurs and Caveman (2017, 2018), March for Science (2017), Rock, Fossil, Quake (2017)